POLITECNICO
MILANO 1863

SCUOLA DI INGEGNERIA INDUSTRIALE
E DELL'INFORMAZIONE

# Satellite System Identification Post-Docking

Tesi di Laurea Magistrale in
Space Engineering - Ingegneria Spaziale

Author: **Giordano Benedetto Ugioli**

Student ID: 968802
Advisor: Prof. Michéle Lavagna
Co-advisors: Stefano Silvestrini, Lorenzo Capra
Academic Year: 2021-22

# Ringraziamenti

Desidero dedicare questo spazio nel mio elaborato a tutti coloro che mi sono stati vicini in questo percorso di crescita personale e professionale.

In primis, un sentito ringraziamento va alla Professoressa Lavagna ed ai Co-relatori Ing. Stefano Silvestrini e Ing. Lorenzo Capra, per l'aiuto ed il supporto fornitomi durante lo sviluppo della Tesi.

Ringrazio infinitamente la mia famiglia, specialmente i miei genitori, Antonella e Roberto, per il loro fondamentale sostegno e presenza nella mia vita.

Desidero infine ringraziare i miei amici e la a mia ragazza, Eleonora per il costante e reciproco supporto.

# Abstract

The present Thesis work deals with the simulation of the attitude dynamical system composed by two spacecrafts after their docking, and as case study, the mission extension between MEV-1 and Intelsat-901 is considered for the simulations.
The final aim of the present work is, in fact, to create, simulate and validate a system identification procedure to determine the mass and mechanical properties of an assembly of already docked satellites.
The problem has been modeled following the rigid body model, which enabled the creation of two dynamical models of increasing complexity: a single body model, which considers the assembly as a whole spacecraft, and a double body model, which considers each spacecraft individually and is used to simulate the attitude dynamics.
The system identification is approached considering a white box model and the family of fitting ode-coefficients as algorithms. The system identification procedure found is divided in five phases, of which the first three phases follow the simplification of the single body model, and are able to retrieve an accurate estimation of the inertia matrix as well as the position of the center of mass of the whole assembly, while the fourth and fifth phase retrieve respectively the inertia properties of each body and the mechanical properties of the link between the two satellites.
The procedure found is then tested in three different environmental conditions: absence of disturbance, Geosynchronous Earth Orbit and Medium Earth Orbit, and the behaviour of the error is evaluated. To assess the robustness of the procedure, a sensitivity analysis has been carried out towards the imprecision of torques and forces and the quality of the angular velocity profile in input.
Finally, the effectiveness is evaluated by conducting a series of control tests to compare the control precision before and after the identification procedures.
**Keywords:** System Identification, Docking, Satellite, White Box, Numerical Methods.

# Sommario

Il lavoro della presente Tesi si occupa della simulazione dell'assetto di un sistema dinamico composto da due veicoli spaziali dopo il loro attracco, e come caso di studio, nelle simulazioni è considerata l'estensione della missione eseguita tra MEV-1 e Intelsat-901.
L'obiettivo finale di questo lavoro è, infatti, di creare, simulare e validare una procedura di identificazione di sistema per determinare le proprietà meccaniche e di massa di un assieme di satelliti attraccati.
Il problema ha preso come riferimento il modello di corpo rigido che ha consentito a sua volta la creazione di due modelli dinamici di complessità crescente: il primo a corpo singolo, che considera l'assiame come un veicolo unico; e un secondo a due corpi, che considera individualmente ogni veicolo spaziale ed è usato per simulare la dinamica di assetto.
L'identificazione del sistema considera un approccio "white box" e la famiglia di algoritmi delle equazioni ordinarie differenziali adattative. La procedura di identificazione del sistema trovata è divisa in cinque fasi, di cui le prime tre seguono la semplificazione del modello di corpo singolo, e sono in grado di fornire una stima accurata della matrice di inerzia e della posizione del centro di massa dell'assieme totale, mentre la quarta e quinta forniscono rispettivamente le proprietà di inerzia dei singoli corpi e le proprietà meccaniche del collegamento fra i due satelliti.
La procedura trovata è successivamente testata in tre condizioni ambientali differenti: assenza dei disturbi, orbita geosincrona terrestre ed orbita terrestre media, così da valutare il comportamento dell'errore. Per stabilire la robustezza della procedura, è stata eseguita un'analisi di sensibilità considerando le imprecisioni di coppie e forze, insieme alla qualità della velocità angolare in ingresso.
Infine, l'efficacia della procedura è valutata tramite una serie di test di controllo per confrontare la precisione del controllo prima e dopo la procedura di identificazione del sistema.
**Parole chiave:** Identificazione del Sistema, Attracco, Satellite, White Box, Metodi Numerici

# Contents

# List of Figures

# List of Tables

# Nomenclature

| Symbol | Definition | Units |
|---|---|---|
| $J_{tot}$ | Inertia Matrix of Assembly | $kg\ m^2$ |
| $w_{tot}$ | Angular velocity of Assembly | $\frac{rad}{s}$ |
| $w_{tot0}$ | Initial angular velocity of Assembly | $\frac{rad}{s}$ |
| $M_{tot}$ | External torque applied on Assembly | $N\ m$ |
| $m_{tot}$ | Mass of the Assembly | $kg$ |
| $I$ | Identity Matrix | - |
| $R_{cm-cm2}$ | Vector distance between $CM_{tot}$ and $CM_2$ | $m$ |
| $J_{1cm}$ | Inertia Matrix of the first body centered on the Assembly CM | $kg\ m^2$ |
| $J_r$ | Inertia coefficient of the sloshing mass of the first body | $kg\ m^2$ |
| $J_{2cm}$ | Inertia Matrix of the second body centered on the Assembly CM | $kg\ m^2$ |
| $J_l$ | Inertia coefficient of the sloshing mass of the second body | $kg\ m^2$ |
| $\dot{\theta_{tot}}$ | Angular velocity of the whole assembly | $\frac{rad}{s}$ |
| $\ddot{\theta_{tot}}$ | Angular acceleration of the whole assembly | $\frac{rad}{s^2}$ |
| $\theta_r$ | Angular position of the sloshing mass of the first body | $rad$ |
| $\dot{\theta_r}$ | Angular velocity of the sloshing mass of the first body | $\frac{rad}{s}$ |
| $\ddot{\theta_r}$ | Angular acceleration of the sloshing mass of the first body | $\frac{rad}{s^2}$ |
| $\theta_l$ | Angular position of the sloshing mass of the second body | $rad$ |
| $\dot{\theta_l}$ | Angular velocity of the sloshing mass of the second body | $\frac{rad}{s}$ |
| $\ddot{\theta_l}$ | Angular acceleration of the sloshing mass of the second body | $\frac{rad}{s^2}$ |
| $\theta_1$ | Angular position of the first body | $rad$ |
| $\dot{\theta_1}$ | Angular velocity of the first body | $\frac{rad}{s}$ |
| $\ddot{\theta_1}$ | Angular acceleration of the first body | $\frac{rad}{s^2}$ |
| $\theta_2$ | Angular position of the second body | $rad$ |
| $\dot{\theta_2}$ | Angular velocity of the second body | $\frac{rad}{s}$ |
| $\ddot{\theta_2}$ | Angular acceleration of the first body | $\frac{rad}{s^2}$ |
| $T$ | Kinetic energy | $\frac{kgm^2}{s^2}$ |
| $U$ | Potential energy | $\frac{kgm^2}{s^2}$ |
| $C_d$ | Damping potential energy | $\frac{kgm^2}{s^2}$ |

| | | |
|---|---|---|
| $V$ | Elastic potential energy | $\frac{kgm^2}{s^2}$ |
| $K$ | Elastic constant vector of the mechanical link | $N\ m$ |
| $C$ | Damping constant vector of the mechanical link | $N\ m\ s$ |
| $C_r$ | Damping coefficient of the sloshing mass of first body | $N\ m\ s$ |
| $C_l$ | Damping coefficient of the sloshing mass of second body | $N\ m\ s$ |
| $M_{c1}$ | Control torque exerted on first body | $N\ m$ |
| $M_{s1}$ | Sloshing torque exerted on first body | $N\ m$ |
| $M_{s2}$ | Sloshing torque exerted on second body | $N\ m$ |
| $M_{ext1}$ | External torque exerted on first body | $N\ m$ |
| $M_{ext2}$ | External torque exerted on second body | $N\ m$ |
| $J_1$ | Inertia Matrix of first body centered on its own CM1 | $kg\ m^2$ |
| $J_2$ | Inertia Matrix of second body centered on its own CM2 | $kg\ m^2$ |
| $CM_1$ | Position of CM of the first body | $m$ |
| $CM_2$ | Position of CM of the second body | $m$ |
| $CM_{tot}$ | Position of CM of Assembly | $m$ |
| $CM_{tot1}$ | Position of CM of Assembly in the first body frame | $m$ |
| $CM_{tot2}$ | Position of CM of Assembly in the second body frame | $m$ |
| $CM_{tot3}$ | Position of CM of Assembly in the whole assembly frame | $m$ |
| $r_{th}$ | Position of thruster | $m$ |
| $F_{th}$ | Force and direction of thruster | $N$ |
| $m_1$ | Mass of the first body | $kg$ |
| $m_2$ | Mass of the second body | $kg$ |
| $\delta t$ | Acceleration time | $s$ |
| $e$ | Eccentricity of the Orbit | - |
| $i$ | Inclination of the orbital plane | $^\circ$ |
| $a$ | Semi-Major axis of the Orbit | $km$ |
| $\omega$ | Anomaly of the perigee | $^\circ$ |
| $\Omega$ | RAAN | $^\circ$ |
| $A_{B/L}$ | Relative attitude between first body frame and LVLH frame | - |
| $A_{B/N}$ | Relative attitude between first body frame and ECI frame | - |
| $A_{B2/N}$ | Relative attitude between second body frame and ECI frame | - |
| $A_{Btot/N}$ | Relative attitude between whole assembly body frame and ECI frame | - |
| $\hat{S}_B$ | Position of the sun in the body frame | - |
| $\rho_s$ | Specular reflectivity coefficient | - |
| $\rho_d$ | Diffuse reflectivity coefficient | - |
| $F_s$ | Solar Radiation | $\frac{kW}{h}$ |
| $\underline{S}_N$ | Position of the Sun in the inertial frame | – |

| | | |
|---|---|---|
| $\underline{m}$ | Residual Magnetic Moment | $Am^2$ |
| $B$ | Magnetic Field | $T$ |
| $A_i$ | Area of surface i | $m^2$ |
| $N_{Bi}$ | Area vector | - |
| $r_{CM-cm1}$ | Vector from $CM_{tot}$ to $CM_1$ | $m$ |
| $r_{cm-th}$ | Vector from $CM_{tot}$ to the thruster position | $m$ |
| $r_i'$ | Generic radius vector form center of mass to point of application of SRP | $m$ |
| $\mu$ | Earth's gravitational constant | $\frac{km^3}{s^2}$ |
| $R_S$ | Distance from Earth to the CM of the Assembly | $m$ |
| $T_{gg}$ | Torque from Gravity Gradient Disturbance | $Nm$ |
| $w_n$ | Natural frequency | $\frac{rad}{s}$ |
| $x$ | State vector for state-space system | $N\ m$ |
| $u$ | Input vector for state-space system | $\frac{rad}{s}\ rad$ |
| $\dot{x}$ | Derivative over time of state vector | $\frac{rad}{s^2}\ \frac{rad}{s}$ |
| $A_{lin}$ | Matrix of dynamics for state-space system | – |
| $B_{lin}$ | Feed-through matrix for state-space system | – |
| $C_{lin}$ | Output matrix for state-space system | – |
| $R_r$ | Reachability matrix | – |
| $Oss_r$ | Observability matrix | – |
| $T_c$ | Control Torque | $N\ m$ |
| $K_p$ | Gain for proportional action in PID control | – |
| $K_p$ | Gain for integral action in PID control | – |
| $w_e$ | Angular velocity error | $\frac{rad}{s}$ |
| $w_{obj}$ | target angular velocity | $\frac{rad}{s}$ |
| $q_c$ | Target quaternion attitude | – |
| $q_e$ | Quaternion error | – |
| $q$ | quaternion vector | – |
| $A_{S/N}$ | Sun pointing attitude matrix | – |
| $\Delta\theta_{max}$ | Maximum angular difference | $rad$ |
| $e_1$ | Eigen axis of rotation | – |
| $\dot{\theta}_{max}$ | Maximum slew rate | $\frac{rad}{s}$ |
| $w_{err}$ | Angular velocity error in tracking control mode | $\frac{rad}{s}$ |
| $w_{lvlh}$ | Angular velocity for LVLH frame | $\frac{rad}{s}$ |
| $A_e$ | Attitude error matrix | – |
| $M_x$ | Torque component of x axis | $N\ m$ |
| $r_y$ | Lever arm component of y axis | $N\ m$ |

# Acronyms

**ADCS** Attitude Determination & Control. 1, 24, 29, 30, 41, 71

**ASIP** After System Identification Procedure. xi, 57, 59, 60, 63–69

**BSIP** Before System Identification Procedure. xi, 57, 59, 60, 62–69

**CM** Center of Mass. xiii, 10, 11, 13, 16, 19–23, 26, 29–31, 41, 43, 45, 49–53, 55, 59

**DBM** Double Body Model. 2, 20–22, 26, 30–32, 51, 58

**DCM** Direction Cosine Matrix. 11

**DoF** Degree of Freedom. 10, 16, 21

**ECI** Earth Centered Inertial. 10, 11

**EM** Electro-Magnetic. 11

**EoM** Equations of Motion. 16, 20–22, 27, 42, 45, 58, 64, 66, 69, 71

**GEO** Geosynchronous Earth Orbit. 1, 2, 12, 35–37, 39, 40, 42–44, 46, 48, 49

**GG** Gravity Gradient. xi, 2, 13, 14

**IGRF** International Geomagnetic Reference Field. 15

**IMU** Inertial Measurements Unit. 31

**LVLH** Local Vertical Local Horizontal. 9–11, 62, 68

**MED** Momentum Exchange Device. 5, 30, 41

**MEO** Medium Earth Orbit. 2, 35–37, 39, 40, 42–44, 46, 48

**MT** Magnetic Torque. xi, 2, 14, 15

**NLP** Non-Linear Programming. 3, 18, 28, 71

**NSO** Numerical Simulation Options. 2, 17

**ODE** Ordinary Differential Equations. 18, 25

**oOS** on Orbit Servicing. 1, 2, 6, 9, 71

**PC** Personal Computer. xiii, 17, 18

**PI** Proportional Integrative. 60, 62

**PID** Proportional Integrative Derivative. 59

**RAAN** Right Acension of the Ascending Node. 9, 10

**SBM** Single Body Model. 2, 20, 21, 26, 27, 38

**SRP** Solar Radiation Pressure. xi, 2, 11–13

# Introduction

On-orbit satellite servicing refers to all activities that provide maintenance, repair, refuelling and mission extension services to a target spacecraft. Considering the history of on Orbit Servicing (oOS), the most important missions have been the Hubble Space telescope servicing missions[8], which allowed to replace and improve the equipment while in orbit. In 2007, the Orbital Express mission[5] was launched, which consisted of two satellites, ASTRO and NEXTsat, being the servicing and serviceable spacecraft respectively, which tested the different phases of docking and the refuelling in orbit. More recently, the MEV-1 and MEV-2 spacecrafts[6] have been launched and will extend the operational life of several satellites in the next years.

In the recent years, an increase in interest for the oOS activities has been recorded. Many satellites in Geosynchronous Earth Orbit are able to operate well beyond their design lives of 15 years, and are decommissioned due to fuel depletion or ageing/malfunction of the Attitude Determination & Control (ADCS) rather than other subsystems. Replacing these "failing" satellites has a great cost in terms of design and launch, while the development of new technologies, such as electric propulsion, allow for the development of economically sound and safe oOS missions, capable of extending the operational life of several different spacecrafts.

Specifically, extending the mission operational lifetime means to dock with the target satellite, and then control the newly formed assembly. To generate an effective control after docking, the knowledge of the whole structure intertial parameters is required, which may either be provided by the ground or retrieved autonomously by the servicing spacecraft.

Parallel to the oOS, the space community has witnessed an increase in interest for more operational autonomy of the spacecraft, since it is essential both for multi-spacecraft missions, to allow for reduced dependency from ground stations, and for the success of deep-space mission with multiple spacecrafts. As a matter of fact, in deep-space the time delay for the communication is significant, and the increase in autonomy would reduce latency and bandwidth constraints[19].

Considering these two raising tendencies in the aerospace sector, the study for Au-

tonomous on Orbit Servicing mission becomes an important research topic. Following this trail, the Work presented in this Thesis aims at defining a system identification procedure to determine the inertial and mechanical parameters of the assembly formed after the docking between the satellites. As benchmark for the procedure found, the analysis of the case study of the mission extension between MEV-1 and Intelsat-901 has been carried out.

The Work of the Thesis is developed through six different chapters. The introduction to the problem, alongside with the description of the satellite assembly composed by MEV-1 and Intelsat-901 is presented in *Chapter 1*.

In *Chapter 2* the environment of the simulation is defined, the external factors that may impact the solution and the frames of reference are specified. Specifically, the orbit model and data are disclosed, together with the environmental disturbance. The Solar Radiation Pressure (SRP), Gravity Gradient (GG), Magnetic Torque (MT) and Sloshing disturbances are presented in detail in this chapter, alongside the Numerical Simulation Options (NSO) used to run the simulation.

The choices made during the modeling of the problem are presented in *Chapter 3*. The two main dynamical models used inside the Work are presented: a first approximated model, defined as Single Body Model (SBM), and a more complex model, Double Body Model (DBM). The first and second model are used inside the system identification procedure, but only the DBM is used to run the simulation.

In *Chapter 4*, the approach to system identification is declared, then the system identification procedure is presented. The procedure is divided in five main phases of increasing complexity, and allow to estimate the mass properties of the spacecrafts.

Inside *Chapter 5*, the system identification procedure is simulated in three different conditions of disturbance: absence, Geosynchronous Earth Orbit (GEO) and Medium Earth Orbit (MEO) to define the robustness of the procedure. The results for each phase and condition are then analyzed. Inside the same chapter, a sensitivity analysis has been carried out considering mismatch in torque and thrust delivery, torque and thrust misalignment, and a sensitivity analysis towards the angular velocity sample error.

To evaluate the utility of the solution provided by the system identification procedure, two control tests are carried out in *Chapter 6*. Specifically, the first control test uses only the parameters available before the system identification procedure, while the second uses the parameters available after the system identification procedure. Each control test is composed by three control modes: inertial pointing, repointing and tracking.

This concludes the Thesis.

# State of the Art

The present Work places itself in the framework of computer simulation studies conducted on the Satellite System Identification and it specifically analyses the situation after the docking between two satellites. The estimation problem of the inertia matrix of a rigid body has been considered in several papers from the aerospace community, with least-squares methods and several different kind of kalman filter being two of the most used methods. For example, in [3] a recursive least-squares method has been considered to identify both inertia matrix and thruster parameters, while in [13] a least correlation method is used to estimate the inertia matrix, and in [15] the inertia matrix is estimated by a constrained least-squares method. Considering the family of kalman filter methods, in [23] extended kalman filter are used to estimate the inertia matrix, while in [16] extended kalman filters are combined with sun sensors, magnetormeters and gyroscopes to determine the attitude of the spacecraft and coupled with a least squares method for estimation of the inertia parameters.
On the contrary, the present work follows the trail of data fitting algorithms, as in [22], which is based on white box model for the system identification approach.
To estimate the inertia matrix and the position of its own center of mass, this Work proposes an out of the box solution, which combines analytical and numerical methods, Non-Linear Programming (NLP) specifically. Moreover a least-squares method is used to estimate the mechanical characteristics of the link between two docked spacecrafts. This results in a procedure that requires only the measure of the angular velocity, requiring no specific sensors or devices. Such characteristics allow the system identification procedure found to be applicable to every kind of spacecraft, regardless of the lifetime and purpose, and to every kind of docking, regardless of the spacecraft sizes and hook type.

# 1 | Chapter 1 - Problem Overview

In this Chapter, the Issue of Research is identified.

## 1.1. Introduction to the Problem

The Work is focused on defining a series of experiments and algorithms which are capable of identifying the properties of a system of two already docked satellites, in terms of inertial data and mechanical properties of the link connecting them.
This means that the objective of the Work is to to provide a procedure capable of delivering an accurate estimation of the inertia properties of the whole assembly, as well as the individual properties of each satellite, together with the mechanical properties of the link connecting the two spacecrafts.
As a clarification note, inside the Assembly of Satellites, the $1^{st}$ Satellite is considered as the Controlling one, hence the terms "$1^{st}$ Satellite" and "Controlling Satellite" will be used throughout the document interchangeably.
To ensure the solution of the System Identification, the complete knowledge of the $1^{st}$ Satellite is considered as given or to be available such as:

- $J_1$: Inertia Matrix of the $1^{st}$ Satellite centered in its $CM_1$
- $CM_1$: Position of Center of Mass of the $1^{st}$ Satellite
- $m_1$: Mass of the $1^{st}$ Satellite
- $r_{th}$: Position of the Thrusters of $1^{st}$ Satellite
- $F_{th}$: Force and Direction of Thrusters of $1^{st}$ Satellite

Due to the broad application of such study, the main driver to define the procedure has been identified in using only sensors and actuators commonly present inside the ADCS suites for spacecrafts: only IMUs, Momentum Exchange Device (MED) and Attitude Thrusters are considered to be available. Moreover, the $2^{nd}$ Satellite is considered as a non-cooperative target, meaning that no data can be transferred between the two Satellites.

## 1.2. Description of the Satellite Assembly

The Satellite Assembly is defined as composed from the $1^{st}$ satellite, the active and controlling one, and by the $2^{nd}$ satellite, which is the non-collaborative and passive satellite, connected by a mechanical Link. It necessary to define not only the inertial properties, but also the orbital data and to quantify disturbing forces in space, which have to be related between them self. To solve this problem, a real mission of on Orbit Servicing has been taken as example. Moreover, this allows to properly test the algorithm in a relevant environment.
The mission chosen is the On-Orbit Servicing mission between the "Mission Extension Veichle one" (MEV-1) and the "Intelsat-901" Satellites. Due to the lack of data for inertial properties, low quality CAD models of both Satellites have been created. For Intelsat 901 size and mass was found in the launch press kit[1] and in [11] for the MEV-1; since no data on the actual size was found for MEV-1, the CAD model used is based on both available pictures and similar spacecrafts sizes, like Intelsat 901. In Fig.1.1 is shown the original render / photos of MEV-1 and Intelsat while in Fig.1.2 are shown the CAD models used.

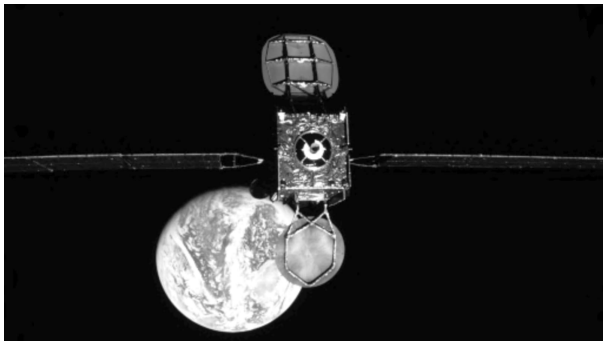

(a) Intelsat 901 as seen from MEV-1 (courtesy of Northrop Grumman)

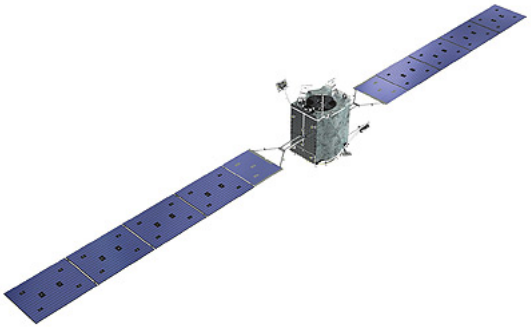

(b) Render of MEV-1 (courtesy of Northrop Grumman)

Figure 1.1: Renders / photos of Intelsat 901 and MEV-1

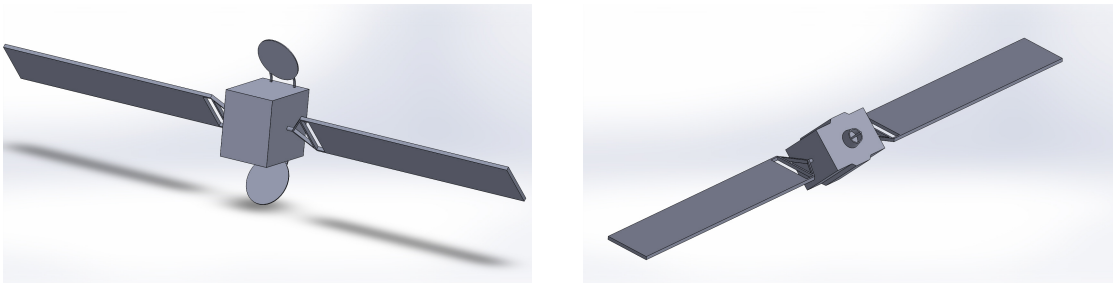

(a) CAD model of Intelsat 901 (b) CAD model of MEV-1

Figure 1.2: CAD model of Intelsat 901 and MEV-1

**Mission Extension** Intelsat 901 is a Communication Satellite equipped with 42 C-band and 14 Ku-band transponders, which was launched on July $9^{th}$ 2001 with a expected operational life of 13 years[2]. In 2019 the Satellite was still perfectly operational but was running low on fuel[12] and was removed from service to be transferred into a graveyard orbit to dock with MEV-1.
Mission Extension Veichle One is a on Orbit Servicing Satellite produced by Northrop-Grumman Group and launched on October $9^{th}$ 2019 with an operational life span of 15 years[6].
MEV-1 and Intelsat 901 docked on February $25^{th}$ 2020 with success, marking an historical first docking between two commercial Satellites[12]. MEV-1 will provide station-keeping and Attitude Control services to the Assembly for a period of 5 year after which Intelsat 901 will be placed into a graveyard orbit and MEV-1 will undock to provide on Orbit Services to other Clients[6].
In Fig.1.3 both the original render and the CAD counterpart of the whole assembly are shown.

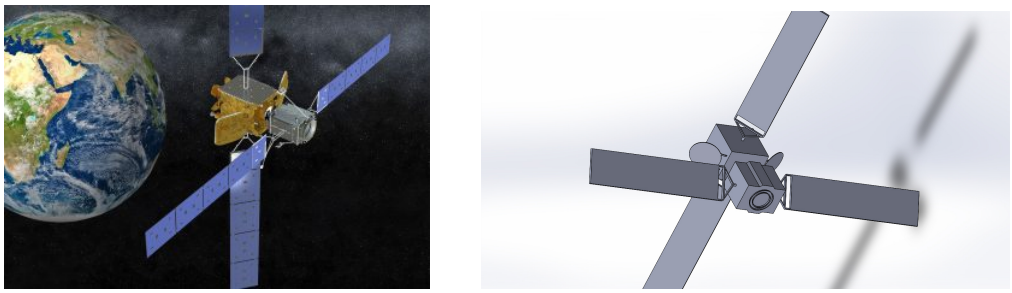

(a) Rendering of the Assembly (b) CAD model of the Assembly

Figure 1.3: CAD & Render of the Assembly of Satellites(courtesy of Northrop Grumman)

# 2 | Chapter 2 - Environment of Simulation & Frames of Reference

Orbital data and model, as well as environmental disturbance models used to simulate the Orbit and Attitude physics are presented in this Chapter, together with the frames of reference used in this Work.

## 2.1. Orbit Model

The orbit model used is a simplified one, from "Orbital Mechanics for Engineering Students" [9], which is useful to determine the position of the Earth, Sun and determine the Local Vertical Local Horizontal (LVLH) frame. Specifically, the model chosen is the restricted 2 Body Problem, in which the true anomaly of the Keplerian parameters is integrated over time. Disturbances affecting the orbit trajectory are not considered, since they do not impact the outcome of the results.
As stated in Section1.2, the orbital parameters chosen are those of the MEV-1 and Intelsat 901 oOS mission and are reported in Tab.2.1. Orbital data used in the orbit simulation is taken after the docking between the two Satellites.

**Orbital Keplerian Parameters**

| Semi-major axis (a) [Km] | Eccentricity (e) [-] | Inclination (i) [deg°] | Anomaly of the perigee ($\omega$) [deg°] | RAAN ($\Omega$) [deg°] |
|---|---|---|---|---|
| 42165 | 0.0002 | 1.64 | 345 | 132 |

Table 2.1: Orbital Parameters, courtesy of [21]

## 2.2. Frames of reference

In this section the main frames of reference used inside the simulation are presented.

### 2.2.1. Earth Centered Inertial Frame

The Earth Centered Inertial (ECI), is the main reference frame used for the simulation, its origin is placed at the center of mass of Earth and its main direction, the x-axis, is defined as the direction of the vernal equinox, while its z-axis is normal to mean equatorial plane of Earth. It is a non-rotating frame of reference. In this thesis it is mainly used to define orbits Degree of Freedom (DoF) (semi-major axis, eccentricity, inclination, anomaly of the perigee, RAAN and true anomaly), the sun direction, as well as the position and velocity of the satellites along the orbit.
Throughout the document, the all terms presented with the subscript $N$, will be referring to the ECI frame (e.g. $S_N$ is the Sun direction in the ECI frame). Furthermore, it is used to create the Attitude body matrix $A_{B/N}$ and the LVLH attitude matrix $A_{L/N}$.

### 2.2.2. Body Frame

The body frame is a reference frame centered in the geometrical center of the controlling spacecraft, and its main direction are parallel to the pitch, roll and yaw rotation axis of the spacecraft. The geometrical center of the first spacecraft is taken as origin of the body frame for two main reasons: the only Attitude knowledge available during the simulation is the one from the controlling satellite and the position of the Center of Mass (CM) may change during the mission.
Throughout the document, the all terms presented with the subscript $B$, will be referring to the Body frame (e.g. $S_B$ is the Sun direction in the body frame). To simulate certain aspects of the underlying physics, another 2 frames were developed; one for the second satellite whose origin corresponds to the CM of the second satellite and aligned with its own pitch, roll ad yaw axis called $A_{B2/N}$. It is important to consider that at rest, the main axis for $A_{B/N}$ and $A_{B2/N}$ are parallel. The second one is used to represent the whole assembly: its origin is set on the $CM_{tot}$ and its axis are aligned as the pitch, yaw and roll axis of the docked spacecrafts, called $A_{Btot/N}$.
To define the attitude body frame over time, the rotations of the satellite are taken into account through the kinematics.

**Kinematics - Quaternions** The purpose of kinematics is to represent the attitude of the spacecraft over time starting from an initial configuration. The attitude is then

propagated from the angular velocity retrieved by the dynamical model. There are many methods to develop the kinematics such as: Direction Cosine Matrix (DCM), Euler angles and Quaternions. Quaternions method has been chosen among the available methods, since during its integration it does not incur in any singularity and are well suited for onboard real-time computation, thus are commonly used[27] to evaluate spacecraft orientation.
Since quaternions do not bear any physical or geometrical interpretation, they have to be converted back into attitude matrix to gain physical meaning. The kinematics for the Passive Satellite are not required in the simulation but have been implemented to check its behaviour over time.

### 2.2.3. Local Vertical Local Horizontal Frame

The Local Vertical Local Horizontal (LVLH) frame is a reference frame defined by the orbit of the spacecraft. Its origin is placed on the CM of the spacecraft, which is followed along the trajectory. Its main direction, x-axis, is defined by the position vector from the CM of the Earth to the CM of the spacecraft, y-axis is directed as the velocity vector and z-axis is normal to the orbital plane.
Throughout the document, all the terms presented with the subscript $L$, will be referring to the LVLH frame (e.g. $S_L$ is the Sun direction in the ECI frame).

## 2.3. Environmental Disturbance

In this section the simulation environment is presented. Disturbing torques that affect the performance of the solution during the simulation are defined. The Numerical integration is defined here as well since it affects the whole simulation, and affects the repeatability of the exact results.

### 2.3.1. Solar Radiating Pressure

Solar Radiation Pressure (SRP) is a disturbing force and torque created by the radiation emitted from the Sun and it acts on both the orbit trajectory and on the attitude of the satellites. In this simulation only the disturbing torque is taken into consideration and, as explained in Sec.2.1, not the effect onto the orbit trajectory. The SRP originates from the interaction between the EM radiation coming from the sun with the surfaces of the

spacecraft.
In this Work, only the contribution from the Sun is considered, since the radiation coming from the planet Earth is very small and can be considered irrelevant due to the high height of the orbit (GEO).
The force of SRP disturbance has been modelled using the following equation[26]:

$$\underline{F}_i = -\frac{F_s}{c} A_i \left(\hat{S}_b \cdot \hat{N_{Bi}}\right) \left[(1-\rho_s)\hat{S_B} + \left(\rho_s \left(\hat{S}_b \cdot \hat{N_{Bi}}\right) + \frac{2}{3}\rho_d\right) \hat{N_{Bi}}\right] \tag{2.1}$$

Where $F_s$ is the Solar Radiation (1358 $[kW/h]$ at Earth's position, while $c$ is the speed of light (3 $10^8$ $[\frac{m}{s}]$). $\hat{S}_B$ is the position of the sun in the body frame, $\hat{N_{Bi}}$ is the individual area normalized vector and $A_i$ is the area of the i-th surface. $\rho_s$ is the specular reflectivity coefficient, estimated to be 0.5, and $\rho_d$ is the diffuse reflectivity coefficient, estimated to be 0.1 for spacecraft body, and 0.8 for the solar panels[18, 25].

To create a correct model of the SRP, the illumination condition has been considered for each surface, and the torque evaluated with a cross product between the lever arm and the force. Since both spacecrafts are free to rotate, the lever arm changes over time. To reflect this variation, the lever arm is defined as:

$$\underline{r}_i = A_{B/N} * A^T_{Btot/N} r_{CM-cm1} + r'_i \tag{2.2}$$

In which $r'_i$ is the distance from the center of mass of the first body to the point of application of the radiating pressure force, while the term $A_{B/N} * A^T_{Btot/N}$ allows to transform the distance between $CM_{tot}$ and $CM_1$ into the system of reference of the first body. The same applies to the second body.
The Sun position has been evaluated in relation with the date of the docking, the $25^{TH}$ of February, which is date of the docking between MEV-1 and Intelsat 901. This allows to consider also the eclipsing condition, which has been modeled as three-dimensional conic shape, thus the conditions for a satellite to see a total eclipse are the same of the transit as seen from a the apex of the shadow cone[26].

**SRP during simulation** To show the behaviour of the SRP disturbance along the orbit, a plot of the torque generated by SRP over time is presented in Fig.2.1, both for the controlling and the passive satellite.

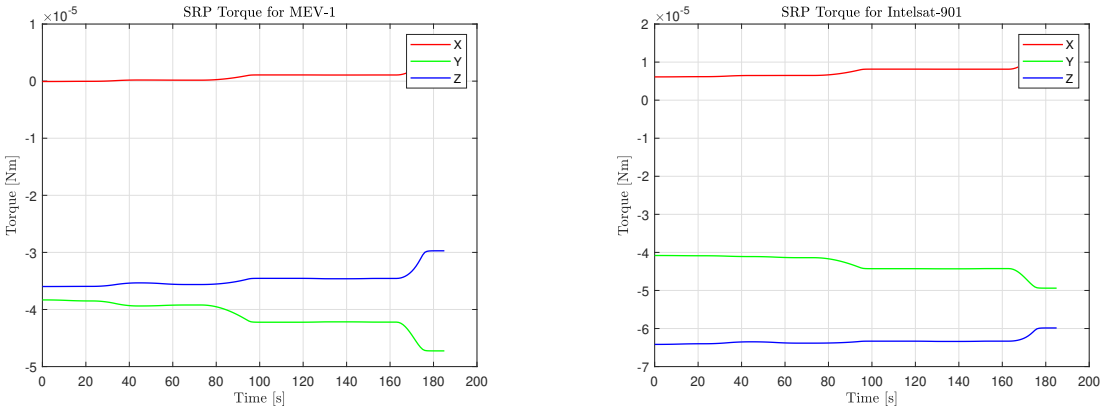


(a) SRP torque for first satellite

(b) SRP torque for second satellite

Figure 2.1: SRP torque over time for both spacecrafts

### 2.3.2. Gravity Gradient

The Gravity Gradient (GG) is a disturbance torque generated by the interaction between Earth's gravity field and a non-symmetrical object of finite dimensions. The model used is simplified and considers the Earth to be a perfect sphere.
The GG has been designed considering the whole Assembly. This allows to correctly evaluate the disturbance equation for each satellite and avoid over or under estimate of the disturbing torque.
The GG is defined as in the book[26]:

$$T_{GG} = \frac{\mu m_{tot}}{R_S^2}(\hat{R}_S \times CM_{tot3}) + \frac{3\mu}{R_S^3}[\hat{R}_S \times (J_{tot}\hat{R}_S)] \tag{2.3}$$

In which $CM_{tot3}$ is the distance from the center of geometry of the Assembly to the $CM_{tot}$, while $R_S$ is the distance from the CM of Earth. To define the torque regarding the first and second body, the properties of each reference frame have to be considered. Considering the vector relations between the geometrical center and the Center of Mass of each frame, and taking into account the definition of Center of Mass (CM), the equation for the GG disturbance torque can be written for each body:

$$\begin{cases} T_{1GG} = \frac{1}{2}\frac{\mu m_{tot}}{R_S^2}(\hat{R}_S \times CM_{tot1}) + \frac{3\mu}{R_S^3}[\hat{R}_S \times (J_{1cm}\hat{R}_S)] \\ T_{2GG} = \frac{1}{2}\frac{\mu m_{tot}}{R_S^2}(\hat{R}_S \times CM_{tot2}) + \frac{3\mu}{R_S^3}[\hat{R}_S \times (J_{2cm}\hat{R}_S)] \end{cases} \tag{2.4}$$

The first term $CM_{tot1}$ is the center of mass expressed in terms of $A_{B/N}$ reference frame and $CM_{tot2}$ in terms of $A_{B2/N}$ reference frame, while $J_{1cm}$ and $J_{2cm}$ are the inertia matrices of

the first and second body, respectively, in the center of mass. The term 1/2 allows to not over estimate the effects of the disturbing torque during the simulation.
In these equations, $R_S$ is the distance from the Earth, and is considered to be the same for each frame, since the distance between frames and the distance from the Earth are of different magnitude order. $R_S$ over time is defined as the matrix product between $A_{B/L}$ and $[1\ 0\ 0]^T$, and $A_{B2/L}$ with $[1\ 0\ 0]^T$ for the first and second satellite respectively.

**GG during simulation** To properly understand the impact of the Gravity Gradient disturbance torque, two plots, one for each spacecraft, show the intensity of the disturbing torque over time during the simulation is shown in Fig.2.2.

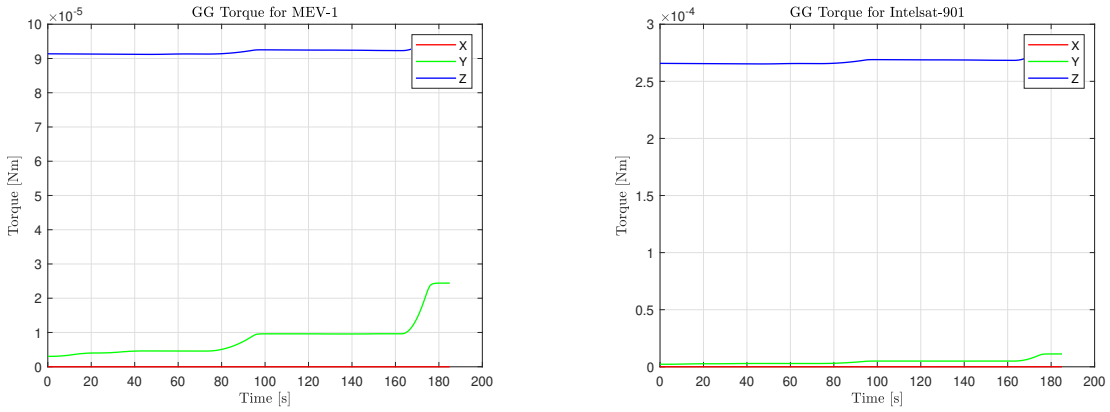


(a) GG torque for first satellite

(b) GG torque for second satellite

Figure 2.2: GG torque over time for both spacecrafts

### 2.3.3. Magnetic Torque

The Magnetic Torque (MT) is a disturbance torque resulting from the interaction between the residual magnetic field of the spacecraft and Earth's magnetic field. Three primary sources are usually identified for the residual magnetic field of the spacecraft but in the Work only the magnetic moments are considered, since the other sources produce negligible effects.
The Magnetic Torque is defined as the cross product between $m_{magn}$, which is the spacecraft magnetic moment and $B$ is the magnetic field in the body frame of each satellite. In Tab.2.2 the values of $m_{magn}$ for each spacecraft are shown.

**Magnetic moments coefficients**

| **MEV-1** $m_{magn1}$ $[Am]$ | **Intelsat-901** $m_{magn2}$ $[Am]$ |
|---|---|
| $[0.01\ 0.05\ 0.01]^T$ | $[0.01\ 0.05\ 0.01]^T$ |

Table 2.2: Magnetic moment for each spacecraft

The Magnetic Field of Earth is similar to the one generated from a dipole, inclined of 10° from the axis of rotation, it is not a fixed field, as a matter of fact it slowly rotates and changes its intensity over time. Hence, models and measures are continuously updated to fit the variations, which are regulated by International Geomagnetic Reference Field (IGRF). The magnetic field is modeled following the magnetic dipole approximation, which can be considered precise for height above 7000 $km$. The dipole model used to simulate the magnetic field is taken from the [26], and the coefficient are taken from the IGRF 2020 model[20].

**Magnetic Torque during simulation** To properly understand the impact of the MT disturbance, two plots, one for each spacecraft, show the intensity of the disturbing torque over time during the simulation is shown in Fig.2.3.

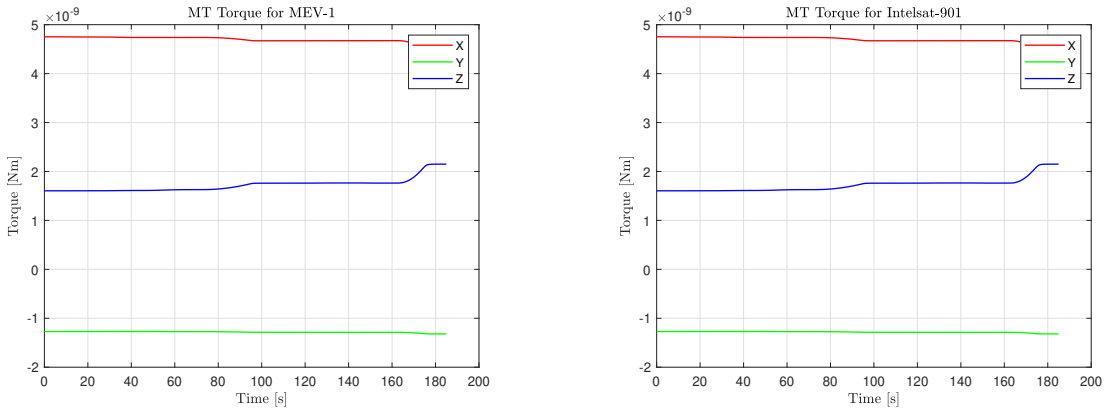


(a) MT torque for first satellite

(b) MT torque for second satellite

Figure 2.3: MT torque over time for both spacecrafts

### 2.3.4. Propellant Sloshing

Propellant sloshing is the disturbance torque generated by the surface oscillations of a fluid in a partially filled tank resulting from angular acceleration of the spacecraft. Sloshing may

persist a long time, due to the low damping from the tank walls. Moreover various factors influence the behaviour of the torque such as the tank geometry, propellant properties and the acceleration field.
The real dynamics of the sloshing inside the tanks of a spacecraft are very complex and outside the purpose of this Work, hence a simplified model has been developed. The effects from sloshing have been treated as the ones from a passive ring dampener, due to the similarities between the systems, thus the dynamic of two ring dampeners were used inside the simulation, one for each spacecraft. The sloshing mass for each spacecraft is considered to have ring shape, with the CM centered as the geometrical centers of each spacecraft and able to rotate only around the yaw axis(Z) of each spacecraft reference frame.
To simulate the sloshing disturbance torque, it necessary to include the dynamics of the ring dampener in the EoM, which are shown in Sec.3.2.2. It is possible to use the equation of Euler-Lagrange and the definition of the Lagrangian, to define the kinetic energy $T$ as:

$$T(\dot{\theta}_r, \dot{\theta}_l) = \frac{1}{2} J_r \dot{\theta}_r^2 + \frac{1}{2} J_l \dot{\theta}_l^2 \tag{2.5}$$

Where $J_r$ and $J_l$ are the inertia of the ring dampeners of the first and second satellite, respectively, $\theta_r$ and $\theta_l$ their DoF.The potential energy $U$ accounts for the damping potential energy from the ring dampeners.

$$\begin{gathered} U(\dot{\theta}_r, \dot{\theta}_l) = C_d(\dot{\theta}_r, \dot{\theta}_l) \\ C_d(\dot{\theta}_r, \dot{\theta}_l) = \tfrac{1}{2} C_r (\dot{\theta}_r - \dot{\theta}_1)^T (\dot{\theta}_r - \dot{\theta}_1) + \tfrac{1}{2} C_l (\dot{\theta}_l - \dot{\theta}_2)^T (\dot{\theta}_l - \dot{\theta}_2) \end{gathered} \tag{2.6}$$

In which $C_r$ and $C_l$ are the damping coefficients of each ring dampener. It is now possible to write the EoM:

$$\begin{cases} J_r \ddot{\theta}_r = C_r(\dot{\theta}_r - \dot{\theta}_1) \\ J_l \ddot{\theta}_l = C_l(\dot{\theta}_l - \dot{\theta}_2) \end{cases} \tag{2.7}$$

The disturbing torque due to sloshing can then be identified as:

$$\begin{cases} M_{s1} = C_r(\dot{\theta}_1 - \dot{\theta}_r) \\ M_{s2} = C_l(\dot{\theta}_l - \dot{\theta}_2) \end{cases} \tag{2.8}$$

which can be included directly in the $M_{ext}$ for each body. In Tab.2.3 the values for the properties related to the sloshing disturbance are presented.

**Sloshing parameters**

| $J_r$ $[Kgm^2]$ | $C_r$ $[\frac{Nm}{s}]$ | $J_l$ $[Kgm^2]$ | $C_l$ $[\frac{Nm}{s}]$ |
|---|---|---|---|
| 1.46 | 30 | 1.04 | 30 |

Table 2.3: Sloshing parameters

**Sloshing during the simulation** To properly understand the impact of the sloshing disturbance torque, two plots, one for each spacecraft, show the intensity of the disturbing torque over time during the simulation in Fig.2.4.

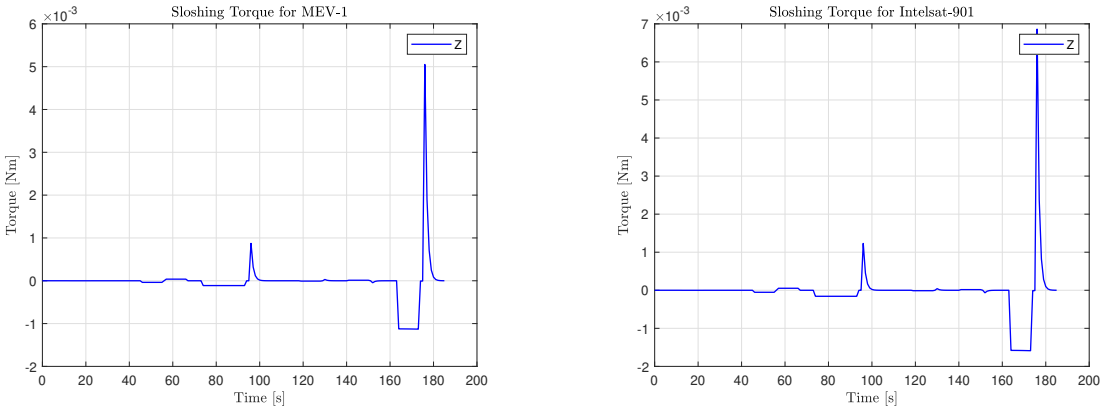


(a) Sloshing torque for first satellite

(b) Sloshing torque for second satellite

Figure 2.4: Sloshing torque over time for both spacecrafts

### 2.3.5. Numerical Simulation Options

In this Section, the Numerical Simulation Options (NSO) are disclosed regarding the Numerical Integration method, the mathematical programming environment used to build and run the simulation, as well as the specifications for the calculator used during the simulation.

**Calculator** To carry out the simulation of the whole system, a Personal Computer (PC) has been used. The PC specifications are reported in Tab.2.4.

**Calculator Specifications**

| | |
|---|---|
| **Processor** | AMD FX-7500 Radeon R7, 10 Compute Cores 4C+6G 2.10 GHz |
| **RAM Installed** | 8 Gb (6.93 Gb usable) |
| **System type** | OS 64 bit based, Processor based on x64 |
| **Operating System** | Windows 10 Home, version 21H2 |

Table 2.4: Specifics of the PC used to develop and run the simulation

**Mathematical Programming Environment** The Mathematical Programming Environment chosen to create and run the simulation are Matlab and Simulink, from Mathworks Company.
Specifically, the Matlab environment is used to generate the input data for the simulation, to elaborate the numerical methods of NLP and to post-process the data into useful plots present in this document.
The Simulink environment is used to properly run the simulations, as a matter of fact the Simulink environment is more suited than the one of Matlab for complex simulations, because it allows to simultaneously integrate different ODE systems. The version used to design and simulate is the Matlab 2021b release.

**Integration method** The Dynamical systems used in this thesis are systems of Ordinary Differential Equations (ODE) from a numerical standpoint. To propagate the behaviour of the ODE over time, numerical integration method are required.
Matlab and Simulink are programming language that come with several built-in function for numerical integration, called ODE solver, being each one useful in different situations. Different solvers have been tested to run the simulation, and *ode45* is the final choice to carry out the simulation. *ode45* is adequate for nonstiff problems and provides a medium accuracy in providing the results. In Tab.2.5 only the different settings from the standard ones for ode45 are presented.

***ode45* Specifications**

| | |
|---|---|
| **Relative Tolerance** | $10^{-3}$ |
| **Absolute Tolerance** | $10^{-6}$ |
| **Zero Crossing Control Algorithm** | Adaptive |
| **Number of Consecutive Zero Crossing** | 1000 |

Table 2.5: List of setting used for ode45

# 3 | Chapter 3 - Approach & Model

In this chapter the model used to elaborate the system identification procedure, as well as to simulate the dynamics is reported.

## 3.1. Modeling choices

The choice of the most suitable model is critical, since it influences the development of the system identification procedure, as well as the results from the tests. Two main approaches can be found, the first one being the rigid body model, and the second being the structural model.

- **Rigid Body Model**: the deformation of the body are not accounted for, which allows to treat the body with a lumped parameters approach, meaning that the properties of a body are defined only by its mass, inertia matrix and CM position. As result, the model provides a first approximation, which is simple to develop and does not require extensive knowledge of the body.
- **Structural Body Model**: the deformation, natural frequency and natural modes are taken into account during the analysis, together with the lumped characteristics of mass, inertia matrix and position of the center of mass derived from the rigid body model. This method allows for a more precise and complex approximation of the behaviour of a real body, but requires the extensive knowledge of the spacecraft, since each part has to be modeled following the structural type of each element (beam, plate for instance).

Considering the issue of research of Sec.1.1, the rigid body model has been chosen for the modeling of the problem for four main reasons:

1. The structural model depends on the data coming from the rigid body model, increasing the priority of this latter model in system identification order.

2. The creation of a proper structural model requires the extensive knowledge of the second spacecraft, which is not available during the system identification.
3. To identify the structure, a distributed suite of sensors would be required all over the Assembly as in [14], which, even if present, would not be available, since the satellites cannot communicate between each other.
4. To include the effects of the mechanical link between the two satellites, the structural model is not required since it is possible to create a lumped parameters representation, since structural elements and contact forces[7] can be treated as spring-dampener systems, and be introduced inside the rigid body model.

## 3.2. Attitude Dynamical Model

In this section the Dynamical Models used both in the solution logic and during the simulation are presented, both in terms of Equations of Motion (EoM) and data.
Two main dynamical models have been developed: the Single Body Model (SBM), which treats the Assembly as a whole body, and a Double Body Model (DBM), which considers the effects of two distinct satellites.
It is important to underline that throughout the simulation the SBM was only used to define the reasoning behind some phases of the system identification procedure, while the DBM has always been used to both simulate the dynamics and to elaborate the phases of the procedure.

### 3.2.1. Single Body Model

The Single Body Model is the first approximation and a reduction of the original problem, in fact the assembly of satellites is considered as a whole. This means that the assembly is identified by a total inertia matrix $J_{tot}$ and a single CM, defined as $CM_{tot}$.
This simplification of the problem is valid only under certain assumptions:

- **Rigid link**: The mechanical link between satellites can be considered as rigid, meaning that:
  - Forces exerted by the controlling satellite induce very small deformations to the Assembly, which can be considered negligible.
- **Negligible Dynamics of Appendages**: Effects from dynamics of Appendages are negligible/non-existent:
  - Appendages are treated as jointed to their main structure.

Starting from the knowledge of the Inertia matrix of the first and second body, $J_1$ and $J_2$ respectively, by using the Hyugens-Steiner theorem it is possible to evaluate both inertia matrices into the Assembly CM, defined as $J_{1cm}$ and $J_{2cm}$ respectively. To properly use the Hyugens-Steiner theorem, the vector distance from $CM_1$ and $CM_2$ to $CM_{tot}$ is required, hence the position of $CM_{tot}$ has to be evaluated using its definition. Then, the total inertia matrix $J_{tot}$ can be found as the sum of $J_{1cm}$ and $J_{2cm}$.
To define the dynamical model, the Equations of Motion (EoM) of the SBM are required. The EoM considered is the Euler equation:

$$J_{tot}\ddot{\theta}_{tot} = J_{tot}\dot{\theta}_{tot} \times \dot{\theta}_{tot} + M_{tot} \tag{3.1}$$

In which $M_{tot}$ accounts for the external couples, such as disturbances and controlling torque, and $\theta_{tot}$ is the DoF.

### 3.2.2. Double Body Model

The Double Body Model is a more refined approximation of the problem, in fact the controlling and the passive satellite are considered as two different bodies and the mechanical connection between them is modeled as a set of 3 rotational springs and 3 rotational dampeners, aligned with the principal axis of the body frame. The Assembly is treated as a multi-body system and its dynamics have to be developed from the CM of the whole Assembly, identified as $CM_{tot}$, thus $J_{1cm}$ and $J_{2cm}$ are used instead of $J_1$ and $J_2$. Moreover, the DoF for which the dynamic is developed are $\theta_1$ and $\theta_2$ which are vector representing the absolute rotation of the first and second satellite, respectively, around the principal axis.
This Dynamical model is considered valid under some assumption:

- **Negligible Relative Translation**: The translation between the First and Second Satellites is considered as negligible/non-existent.
  - The relative position between $CM_{tot}$, $CM_1$ and $CM_2$ is fixed over time.
- **Negligible Dynamics of Appendages**: Effects from dynamics of Appendages are negligible/non-existent:
  - Appendages are treated as jointed to their main structures

The Dynamical model for the DBM can be found starting from the equation of Euler-Lagrange and the definition of Lagrangian. The kinetic energy $T$ is defined as:

$$T(\dot{\theta}_1, \dot{\theta}_2) = \frac{1}{2} J_{1cm} \dot{\theta}_1^T \dot{\theta}_1 + \frac{1}{2} J_{2cm} \dot{\theta}_2^T \dot{\theta}_2 \tag{3.2}$$

The potential energy $U$ is defined as the sum of the potential elastic energy $V$ and potential damping energy $C_d$:

$$\begin{gathered} U(\theta_1, \dot{\theta}_1, \theta_2, \dot{\theta}_2) = V(\theta_1, \theta_2) + C_d(\dot{\theta}_1, \dot{\theta}_2) \\ V(\theta_1, \theta_2) = \tfrac{1}{2} K(\theta_2 - \theta_1)^T (\theta_2 - \theta_1) \\ C_d(\dot{\theta}_1, \dot{\theta}_2) = \tfrac{1}{2} C(\dot{\theta}_2 - \dot{\theta}_1)^T (\dot{\theta}_2 - \dot{\theta}_1) \end{gathered} \tag{3.3}$$

Then the EoM in tensorial form for the DBM can be evaluated:

$$\begin{cases} J_{1cm} \ddot{\theta}_1 = J_{1cm} \dot{\theta}_1 \times \dot{\theta}_1 + K(\theta_2 - \theta_1) + C(\dot{\theta}_2 - \dot{\theta}_1) + M_{c1} + M_{ext1} \\ J_{2cm} \ddot{\theta}_2 = J_{2cm} \dot{\theta}_2 \times \dot{\theta}_2 + K(\theta_1 - \theta_2) + C(\dot{\theta}_1 - \dot{\theta}_2) + M_{ext2} \end{cases} \tag{3.4}$$

Inside the EoM the terms of $M_{ext1}$ and $M_{ext2}$ represent the disturbing torques on the first and second satellite, while $M_{c1}$ represent the control torque acting on the controlling satellite.
This dynamical model underlines properties and quality of the mechanical link expressed in terms of elastic and damping properties, represented respectively by $K$ and $C$ inside the equation.

### 3.2.3. Body Data

In this subsection the relevant data required to simulate the dynamical model are presented, together with the initial conditions considered and required for integration.
The Inertia matrices, referred to the CM of their respective bodies are defined as:

$$J_1 = \begin{bmatrix} 15349.21 & 0.00 & -39.04 \\ 0.00 & 2954.76 & 0.00 \\ -39.04 & 0.00 & 15827.90 \end{bmatrix} \; and \; J_2 = \begin{bmatrix} 14770.95 & 39.04 & 0.00 \\ 39.04 & 14526.33 & 0.00 \\ 0.00 & 0.00 & 4092.54 \end{bmatrix} \tag{3.5}$$

The mass of each Satellite and the position of their CM with respect to the body frame, is shown in Tab.3.1.

**Mass & CM position**

| | **Mass** $[kg]$ | **CM** $[m]$ |
|---|---|---|
| **MEV-1** | 2326 | $[0.5\ 0.4\ -0.3]^T$ |
| **Intelsat 901** | 1972 | $[3.2\ 0.3\ -0.4]^T$ |

Table 3.1: Mass and position of CM of each Satellite

Applying the Hyugens-Steiner Theorem it is possible to evaluate $J_{1cm}$ and $J_{2cm}$:

$$J_{1cm} = \begin{bmatrix} 15359 & 132 & 93 \\ 132 & 6529 & -4 \\ 93 & -4 & 19402 \end{bmatrix} \quad and \ J_{2cm} = \begin{bmatrix} 14782 & 194 & 155 \\ 194 & 18742 & -5 \\ 155 & -5 & 8308 \end{bmatrix} \tag{3.6}$$

Using the calculation shown in Sec.3.2.1 the $CM_{tot}$ and $J_{tot}$ are evaluated and presented in Tab.3.2.

**Mass, CM position and Inertia Matrix**

| **Mass** $[kg]$ | **CM** $[m]$ | **Inertia Matrix** $[kg\ m^2]$ |
|---|---|---|
| 4298 | $[1.73\ 0.35\ -0.35]^T$ | $\begin{bmatrix} 30141 & 327 & 249 \\ 327 & 25271 & -10 \\ 249 & -10 & 27711 \end{bmatrix}$ |

Table 3.2: Mass, position of CM and inertia matrix of the whole Assembly

The mechanical properties of the mechanical link have been chosen keeping in mind that a generic link between satellites should be designed as rigid as possible, with high stiffness as priority. As a matter of fact a very stiff link would allow to treat the Assembly of satellites as a whole, simplifying the control laws required. Values used in the simulation are shown in Tab.3.3.

**Visco-elastic coefficients**

| **Elastic Coefficient** $K$ $[\frac{Nm}{rad}]$ | **Damping Coefficient** $C$ $[\frac{Nm\ s}{rad}]$ |
|---|---|
| $[1200000\ 700000\ 850000]^T$ | $[90000\ 80000\ 110000]^T$ |

Table 3.3: Elastic and Damping coefficient

**Initial Conditions** To properly carry out a full simulation, the initial values are required. The initial value chosen for each element of the Eq.3.4 are presented in Tab.3.4, together with the initial Attitude matrix.

**Initial values**

| | |
|---|---|
| $\theta_1\ [rad]$ | $[0\ 0\ 0]^T$ |
| $\dot{\theta}_1\ [\frac{rad}{s}]$ | $[0\ 0\ 0]^T$ |
| $\theta_2\ [rad]$ | $[0\ 0\ 0]^T$ |
| $\dot{\theta}_2\ [\frac{rad}{s}]$ | $[0\ 0\ 0]^T$ |
| $A_{B/N}$ | $\begin{bmatrix} 1 & 0 & 0 \\ 0 & 1 & 0 \\ 0 & 0 & 1 \end{bmatrix}$ |

Table 3.4: Initial conditions for the Simulation

## 3.3. Unmodeled factors

The Work presented in this Thesis concentrates on the system identification, hence many factors, which are usually included in a Attitude Determination & Control (ADCS) simulation are not kept into account. Factors such as:

- **Sensors internal dynamics** : there exist very different kind of sensors with a wide range of accuracy and noise, together with a series of techniques to increase precision and reduce noise. Avoiding the modeling of internal dynamics allows to obtain general results applicable to a wider range of spacecrafts.
- **Attitude determination algorithms** : similarly to sensors internal dynamics, many techniques are available to increase the accuracy and filter the noise, and avoiding the selection of a certain method allows to obtain more general results applicable to a wider range of spacecrafts.
- **Actuators internal dynamics** : different kinds of actuators are available in the market, and each one has different internal dynamics. Considering the torque acting on the spacecraft as direct product of the control, allows to create a more general model applicable on a wider range of spacecrafts. The internal dynamics of the actuator has been considered only when it impacted or produced interesting results for the system identification procedure or to support reasoning and choices made.

# 4 | Chapter 4 - System Identification Procedure

In this chapter the system identification procedure found is presented.

## 4.1. System Identification approach

The System Identification is a branch of science which focuses on finding a suitable model structure to build mathematical models, as well as to design experiments to fit a certain model. Three main approaches can be identified:

- **Black Box Model**: no insight is available of the internal dynamics, and a flexible dynamical model structure is chosen to fit the data.
- **Gray Box Model**: some insight is available for part of the internal dynamics, but several parameters remain to be determined from data.
- **White Box Model**: the internal dynamics is perfectly known, and is constructed from first principles.

Considering that the basic rule in estimation is *"not to estimate what you already know"*[24], and that the dynamical model of the attitude of a spacecraft is known and reported in Sec.3.2.1 and Sec.3.2.2, a white box model has been chosen as approach for the system identification.
Considering the communities around the core of system identification[17], to set the algorithms and make critical choices during the development of the Work, the procedure presented onward belongs to the family of "Fitting ODE-coefficients". In fact this family of algorithms takes advantage of the physical modeling, involving numerical methods for the solution of Ordinary Differential Equations systems, which well fit the white box approach selected for the system identification approach.

## 4.2. Introduction to the Solution Logic

As stated in Ch.1, the Solution Logic is a procedure divided in phases capable to identify the mechanical and mass properties of a system of already docked satellites. The workflow of the procedure is presented into the next paragraph, and is here shortly summed up. The idea behind the procedure, is to firstly identify the mass properties of the whole assembly by using a simplified dynamical model (SBM), then the properties of the connection between satellites are retrieved from using a more complex dynamical model (DBM). This can be done given the full knowledge of the first satellite, as specified in Sec.1.1.

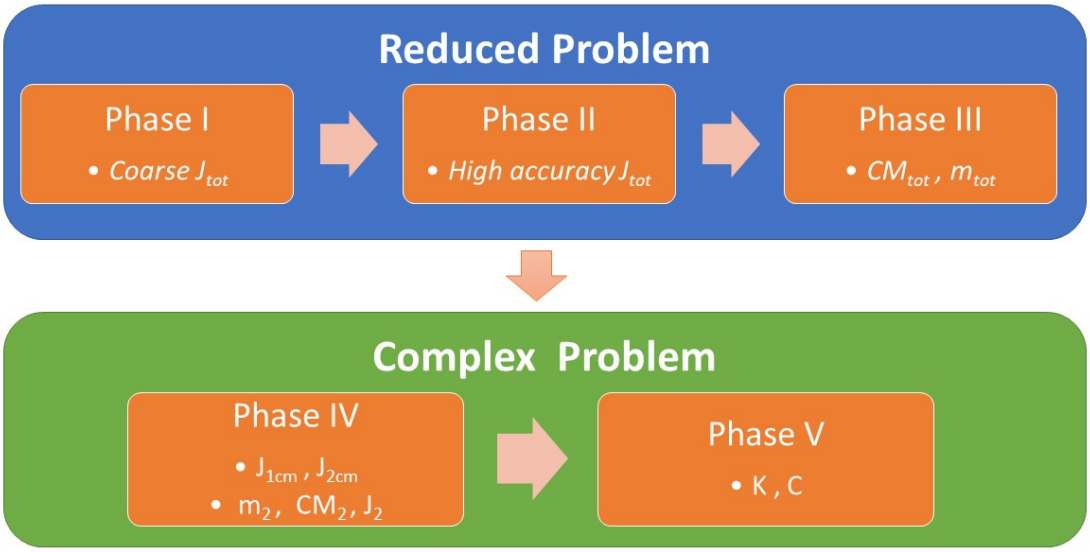


Figure 4.1: Solution Logic workflow

**Workflow** The procedure is divided in 5 phases, the first three phases follow the hypotheses of the reduced problem and their results are used in the remaining fourth and fifth phase, which follow the complex problem model. The workflow starts with a set of small perturbations aimed at generating a coarse estimation of the assembly inertia matrix $J_{tot}$, while in the second phase a more precise estimation of the inertia matrix is retrieved starting from the coarse value. With the accurate knowledge of $J_{tot}$, it is possible to evaluate the position of the CM and the total mass of the assembly by executing two angular accelerations involving thrusters. The knowledge of the CM and $J_{tot}$ allows to find the individual inertia matrices of the spacecrafts, and the $m_{tot}$ can be used to find the $m_2$(mass of the second body), $CM_2$ (center of mass of the second body) and $J_2$ (Inertia

Matrix of the second body in its own $CM_2$). At this point it is possible to define a final test to retrieve the characteristics of stiffness $K$ and damping $C$ related to the mechanical link. The workflow is schematized in Fig.4.1.

## 4.3. Reduced Problem

The Reduced Problem Solution Logic, considers the Assembly as a whole spacecraft and uses the Single Body Model as dynamical model reported in Sec.3.2.1. Moreover, due to the hypothesis behind the SBM, the angular velocity sampled from the first satellite can be considered as the angular velocity of the whole satellite.

### 4.3.1. Phase I - Coarse Inertia

In the first phase of the system identification procedure, the Assembly is perturbed by small torques. As a matter of fact, if the rotation velocity are small enough, the term $J_{tot}w_{tot} \times w_{tot}$ inside Eq.3.1, which is a highly non linear term, becomes negligible and the EoM of the Assembly change from Eq.3.1 to:

$$J_{tot}\dot{w}_{tot} = M_{tot} \tag{4.1}$$

The Eq.4.1 presents linearity between angular accelerations $\dot{w}_{tot}$ and the Torques applied $M_{tot}$ to the Assembly. It can be considered that if the acceleration is linear, then there exist a linearity between acceleration and velocity, thus the torque applied and the angular velocity become linearly dependent:

$$w_{tot} = J_{tot}^{-1}M_{tot}\Delta t + w_{tot0} \tag{4.2}$$

Which is the kinematic equation for angular motion and $w_{tot0}$ is the initial angular velocity. Since the system can be defined as linear, it is possible to accelerate and brake the system, if the accelerating and braking torque are equal, contrary and applied for the same amount of time.
Thanks to this property, it is possible to create a set of 3 tests (one for each axis), in which a single torque on a single axis can be exerted at a time, and by evaluating the final angular velocity on the three axis, it is possible to determine the various components of $J_{tot}$. If the initial angular velocity $w_{tot0}$ is zero, the Eq.4.2 can be rewritten in the form:

$$J_{tot}^{-1} = (M_{tot}\Delta t)^{-1}w_{tot} \tag{4.3}$$

Using the final value of angular velocity, the torque and time at the end of each acceleration test, it is possible to evaluate the matrix of coefficients of $J_{tot}^{-1}$. Considering that the $J_{tot}^{-1}$ matrix is symmetric and full rank, it is possible to evaluate the inverse $J_{tot}$.

### 4.3.2. Phase II - Refined Inertia

In the second phase of the system identification procedure, a more complex and accurate analysis is carried out, with the aim of increasing the estimation precision of the inertia matrix $J_{tot}$. Differently from the phase I, the phase II takes advantage of the non-linearity of the dynamical system by applying a set of constant torques to the Assembly. This makes the term $J_{tot}w_{tot} \times w_{tot}$ inside Eq.3.1 more relevant, which is the main origin of non-linearities in the system. During the acceleration, the angular velocity profile is sampled and taken as parameter to be used inside the algorithm.
The Algorithm used is called "Inertia Refiner", uses a NLP numerical method with the inertia matrix $J_{tot}$ as optimization parameter and the coarse inertia matrix from the simple tests as initial guess. The cost function is defined as the error between the sampled and propagated profile of angular velocity during the acceleration. Then the cost function is elaborated by a numerical method, specifically a constrained optimizer, to enforce the symmetry property of the inertia matrix. In this way the optimizer iterates the inertia matrix to better fit the velocity profile, this allows to filter out the disturbances and improve the knowledge of the inertia matrix.
To implement the numerical method, Matlab offers different built-in functions to solve NLP problems. Since both objective function and constrains are continuous function with continuous first derivative, *fmincon*, a gradient-based numerical method, has been chosen to carry out the optimization. Specifically *fmincon* can use different algorithms, to adapt itself better to the problem, and *interior-point* was selected, since it can handle large, sparse problems and satisfy the boundaries at every iteration. The Inertia Refiner pseudo algorithm is presented in Alg.4.1.

Algorithm 4.1 Inertia Refiner

1: Acceleration
2: Sampling of angular velocity
3: *Use of the Constrained Optimizer*
4: **while** Costfun($J_{tot}$) >= Tolerance **do**
5: Generate new $J_{tot}$
6: *Check constrains are satisfied*
7: Propagation of angular velocity based on new $J_{tot}$
8: Error evaluation of angular velocity profile
9: **end while**

Once the refined version of the inertia matrix is obtained, the system can be stopped by using a detumbling control law.

### 4.3.3. Phase III - Center of Mass

While the inertia matrix impacts every aspect of the angular velocity, the position of the Center of Mass (CM) of the spacecraft defines the torque deriving from the force applied to the spacecraft. As a matter of fact, the torque acting on a mechanical system is defined as the cross product between the lever arm and the force vector.
To estimate the position of the CM, it is then required to perform a test involving forces to exploit the CM properties. On a spacecraft, the most suitable actuator to carry out such test are the thrusters from the ADCS, which can either be used to directly control the attitude of the spacecraft or help unloading the wheels[26]. Using the same reasoning of the first phase of the procedure, it is possible to perturb the Assembly and keep a linear relation between torque and angular velocity as in Eq.4.2, and in this case, this property can be used to evaluate the torque applied to the system, which can be used to retrieve the lever arm between the CM and the position of the thruster.

$$M_{tot} = (J_{tot}^{-1}\Delta t)^{-1} w_{tot} \tag{4.4}$$

Due to the nature of the cross product, even with the knowledge of the torque and force applied, it is not possible to recover the lever arm, if the force is oriented in a generic direction. However, if the force applied is parallel to one of the principal axis, and it becomes possible to evaluate the lever arm of the two remaining axis. As an example, if a thruster is fired parallel to axis X, the knowledge of the lever arm in terms of Y and Z

coordinate becomes available:

$$\begin{bmatrix} M_x \\ M_y \\ M_z \end{bmatrix} = \begin{bmatrix} 0 \\ r_z \ F_x \\ -r_y \ F_x \end{bmatrix} \tag{4.5}$$

Due to this characteristic, two tests, with different thrusters, placed in the same position, firing in two different direction, are required to fully determine the lever arm between the CM and the thruster.
Once the lever arm is known, it is possible to evaluate the position of CM. Since the position of the thrusters is known (belonging to the first body), retrieving the position of the CM is a matter of vector sum:

$$CM_{tot} = r_{th} - r_{cm-th} \tag{4.6}$$

Where $r_{th}$ is the position of the thruster from the center of the reference frame.
It must be noted that to perform such tests, Momentum Exchange Device (MED) are required to brake the system at the end of each acceleration, since it is not possible to directly control the resulting torque from thrusters without the knowledge of the CM. This means that the momentum generated by the tests is loaded onto the MED during braking. This increases the risks related to momentum saturation of the MED and the consequential loss of functionality of the ADCS which can result in harming the mission's success.

**Real torque** As previously discussed in Sec.2.3.1, the lever arm during the simulation of the real system is considered as in Eq.2.2, which can be rewritten as:

$$\underline{r}_i = A_{B/N} * A^T_{Btot/N} r_{CM-cm1} + r_{th} \tag{4.7}$$

Which allows to consider the relative rotation between the Assembly reference frame and the one of the bodies.

## 4.4. Complex Problem

The Complex Problem Solution Logic considers the Assembly as two different bodies, the first and second satellite, and uses the Double Body Model as dynamical model, which is reported in Sec.3.2.2. The objective of this section of Solution Logic is to identify the characteristics of the mechanical link between the two satellites in terms of stiffness and damping.

### 4.4.1. Phase IV - Docked spacecrafts properties

Once the mass properties of the whole Assembly are known, it is possible to retrieve the mass properties of each satellite. First of all it is possible to evaluate the $J_{1cm}$ (inertia matrix of first satellite in $CM_{tot}$), with the Hyugen-Steiner theorem, since the knowledge of $m_1$, $r_{cm1-cm}$ and $J_1$ are known. Then it is possible to calculate $J_{2cm}$, which is the Inertia Matrix of the second body positioned in $CM_{tot}$, as the difference between $J_{tot}$ and $J_{1cm}$. Specifically $J_{1cm}$ and $J_{2cm}$ are required to evaluate the Double Body Model (DBM) in the next phase of the procedure, because mechanical systems have to be developed starting from the CM of the whole Assembly, in this case $CM_{tot}$.

### 4.4.2. Second satellite system identification

Additional information about the mass properties of the second body, such as $m_2$, $CM_2$ and $J_2$, can be retrieved. These are defined as additional information, since they are not required to simulate/control the whole Assembly. Considering the third phase of the system identification procedure, the linear acceleration during the thruster firing is sampled by the on-board accelerometers, which are usually present in the IMU, together with gyroscopes, which are required for the angular velocity measures.
From the second principle of dynamics it is known that the force is proportional to the mass times the acceleration.
The acceleration is given from the IMU, while the Force is either known from the specifics of the thrusters or from the throttling level selected, thus it is possible to recover the $m_{tot}$. Then the mass of the second satellite, $m_2$, is found as the difference between $m_{tot}$ and $m_1$. Once $m_2$ is found, it is possible to use the definition of center of mass and retrieve $CM_2$ :

$$CM_2 = \frac{CM_{tot}m_{tot} - CM_1m_1}{m_2} \tag{4.8}$$

It is now possible to apply the Hyugens-Steiner theorem and retrieve $J_2$:

$$J_2 = J_2cm - m_2[(R_{cm-cm2} \cdot R_{cm-cm2})I - R_{cm-cm2} \otimes R_{cm-cm2}] \tag{4.9}$$

It is important to point out that this test is just speculative and not evaluated inside the simulator. As a matter of fact inside the simulation the acceleration would have been evaluated with the second principle of the dynamics, hence the total mass would have ended up in a perfect result each time, rendering useless the need for a simulation. Moreover the data obtained in this way is not relevant for the mass properties of the docked spacecrafts, which is the objective of this work.

### 4.4.3. Phase V - Visco-Elastic Fitting

The fifth phase of the system identification procedure is similar to the second phase, presented in Sec.4.3.2. As a matter of fact, it takes advantage of the non-linearity coming from both dynamical system and the mechanical link. Using a set of constant but different torques it is possible to make the terms $J_{1cm}\dot{\theta}_1 \times \dot{\theta}_1$, $J_{2cm}\dot{\theta}_2 \times \dot{\theta}_2$, $K(\theta_2 - \theta_1)$ and $C(\dot{\theta}_2 - \dot{\theta}_1)$ more relevant in Eq.3.4, which are the main source of non-linearities in the DBM.

Before the start of the acceleration, the spacecraft has to be stopped, in this way the initial condition for both spacecraft are know. Specifically, the difference in angular velocity, which regulates viscous phenomena, and the angular difference, which regulates the elastic phenomena, between the two satellites can be assumed as zero. This is fundamental, since no information is available on the state of the second satellite. The Assembly of spacecraft is then accelerated by a set of torques, and the angular velocity profile of the first satellite is sampled and taken as parameter to be used inside the Algorithm.

The Algorithm is called "Visco-Elastic Fitting", and uses a numerical method with the elastic parameter $K$ and viscous parameter $C$ as optimization variable. Similarly to the second phase, the cost function is defined as the error between the sampled and the propagated profile of angular velocity of first body during the acceleration. To be specific, the propagation uses the DBM, using Eq.3.4 to simulate the dynamics. The cost function is optimized by a numerical method, in this case a nonlinear least-squares solver which allows to evaluate the error along time. This algorithm allows to iterate different times the values of $K$ and $C$, resulting in adequate fitting of the velocity profile of the first body.
To implement the numerical method, the Matlab built-in functions have been used, specifically *lsqnonlin*, which allows to solve nonlinear least-squares curve fitting problems, running *trust-region-reflective* as algorithm.
The "Visco-Elastic Fitting" pseudo algorithm is presented in Alg.4.2.

Algorithm 4.2 Visco-elastic Fitting

1: Acceleration
2: Sampling of angular velocity of first body
3: *Use of the Least squares Optimizer*
4: **while** Costfun($C$ & $K$) >= Tolerance **do**
5: Generate new $C$ & $K$
6: Propagation of angular velocity based on new $C$ & $K$
7: Error evaluation of angular velocity profile of first body
8: **end while**

During the development of the Work, some peculiarities have arisen while researching this algorithm, which define the field of application of this method, specifically:

**Rigid Body Threshold** : The stiffness and damping coefficients must be compatible with the order of magnitude of the inertia matrix. Otherwise the Optimizer cannot converge to a solution.
Compatibility is intended as belonging to a neighborhood with roughly the size of 3 orders of magnitude around the diagonal Inertia Matrix values. The neighborhood limit is defined as the Rigid Body Threshold, since beyond a certain threshold of values of $K$ and/or $C$ the system response does not change significantly. Specifically, this is due to the fact that the system behaves like a whole rigid body. In return, the small difference in system response makes the optimizer unable to converge, reducing its sensibility to error.

**Initial guess not required** : It is not required to produce a reasonable initial guess for $K$ and $C$ for the optimizer to converge, but it is necessary that the initial guess respects the condition of rigid body threshold. As a matter of fact, the initial guess for the optimizer can be taken from the $J_{tot}$ main diagonal to speed up the optimizer process. This allows to avoid extra costs of a new set of tests or specific sensors to generate the initial guess.

# 5 | Chapter 5 - Simulation and Results of the Procedure

In this chapter the simulation and results obtained from the system identification procedure of Ch.4 are presented and analyzed together with the choices made when performing the tests. For each test the results coming from the ideal case, without disturbances, together with the ones from the real case, typical disturbances of GEO, are presented. To prove the effectiveness of the procedure, an additional simulation has been carried out considering the environmental disturbances in a MEO and presented alongside the main results. As a matter of fact, in the GEO environment, some disturbing torques are reduced due to the greater height from the surface of planet Earth. For the MEO, a semi-major axis of 1500 $km$ has been considered, while the remaining orbital parameters are unchanged.

## 5.1. Phase I - Coarse Inertia

The estimation of the inertia matrix for the whole assembly requires three tests to be performed, one for each axis. To correctly perform these tests, some parameters such as controlling torque and acceleration time have to be tuned to improve the quality of the results. Specifically:

**Torque** The torque applied to the assembly by the first satellite, shall be some order of magnitude higher than the order of magnitude of the disturbances, in this way the angular velocity at the end of acceleration can be considered as direct result of the controlling action, while the contribution from the disturbing torque becomes negligible. At the same time, using a greater torque increases the risk of exciting non-linearities either from the dynamics or either from the visco-elastic vibration of the mechanical link. Considering these upper and lower limits, the value of 1 $Nm$ has been chosen for the control torque during each test.

**Acceleration Time** Similarly to the torque, the acceleration time has upper and lower limits. As lower limit, the acceleration time shall last for an amount of time compatible with the disturbing and controlling torques, such that the angular velocity can be considered as direct result of the controlling action. On the contrary, non-linearities from dynamics can arise over time, thus the acceleration time shall be short enough to avoid them. Given these limits, a good compromise for acceleration time has been found as 10 $s$.

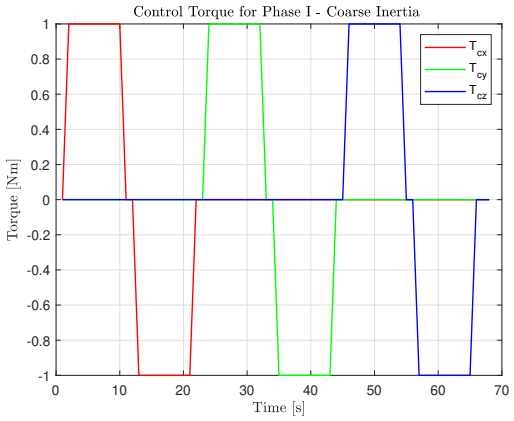


Figure 5.1: Control torque over time for Phase I - Coarse Inertia

Before showing the final results of the test procedure, the torque profile used for every simulation is presented in Fig.5.1, while the angular velocity over time for GEO and MEO cases are shown in Fig.5.2. Angular velocity profile in absence of disturbances is not show since it is too similar to the one of the GEO case, and no major difference are present.
It is interesting to notice the linearity between the torque and angular velocity, which validates the solution logic of Sec.4.3.1. In Fig.5.2b it is possible to evaluate the impact of the disturbances during the braking phase and see that they impact the ability of the system to reach zero angular velocity and that error gets accumulated over time and it is not rejected between accelerations.

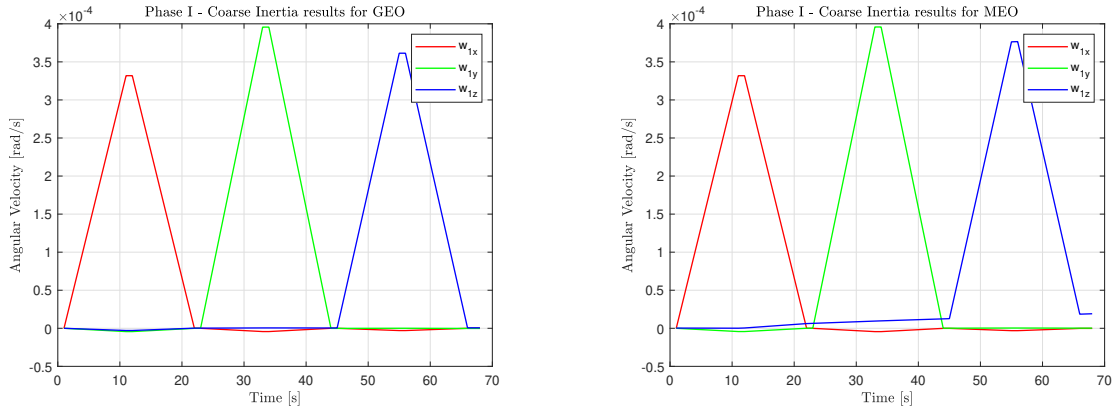


(a) GEO case (b) MEO case

Figure 5.2: Angular velocity over time for Phase I - Coarse Inertia

The final results of Phase I - Coarse Inertia are presented in Tab.5.1. To appreciate the overall difference with the presence of disturbances, the error has been evaluated in three ways:

1. **Plain Error**: Plain difference between the original and estimated inertia matrix
2. **Diagonal Error**: Norm of the diagonal elements of the Plain Error matrix
3. **Extradiagonal Error**: Norm of the extradiagonal elements of the Plain Error matrix

**Inertia Matrix results**

| | **Inertia Matrix** $[Kgm^2]$ | **Plain Difference** $[Kgm^2]$ | **Diagonal Error** $[Kgm^2]$ | **Extra-Diagonal Error** $[Kgm^2]$ |
|---|---|---|---|---|
| **Without Disturbances** | $\begin{bmatrix} 30141 & 326 & 249 \\ 326 & 25271 & -10 \\ 249 & -10 & 27711 \end{bmatrix}$ | $\begin{bmatrix} 0.008 & 0.303 & 0.012 \\ 0.303 & 0.585 & -0.47 \\ 0.012 & -0.47 & 0.001 \end{bmatrix}$ | 0.5 | 0.55 |
| **With GEO Disturbances** | $\begin{bmatrix} 30141 & 329 & 247 \\ 329 & 25277 & -31 \\ 247 & -31 & 27674 \end{bmatrix}$ | $\begin{bmatrix} 0.12 & -2.03 & 1.40 \\ -2.03 & -5.6 & 20.9 \\ 1.40 & 20.9 & 36.62 \end{bmatrix}$ | 37.04 | 21.04 |
| **With MEO Disturbances** | $\begin{bmatrix} 30143 & 319 & 240 \\ 319 & 25281 & -634 \\ 240 & -634 & 26590 \end{bmatrix}$ | $\begin{bmatrix} -2.03 & 7.45 & 8.46 \\ 7.45 & -9.51 & -623 \\ 8.46 & -623 & 1120 \end{bmatrix}$ | 1120 | 623.7 |

Table 5.1: Results from Phase I - Coarse Inertia

Considering these results, there is a clear relation between the environmental disturbances level and the accuracy of the solution. Considering the plain difference, it is possible to note that as the disturbances increase in magnitude, the error on the estimation of the $I_{zz}$ and $I_{yz}$ component increases significantly, and drive the rise of the diagonal and extra-diagonal error. The origin of this behaviour can be found considering Fig.5.2b, where the starting angular velocity for the third acceleration, which is around the z-axis, is not zero due to the presence of disturbances.

## 5.2. Phase II - Refined Inertia

The high quality estimation of the inertia matrix for the whole assembly requires a single test, which exploits the non-linear components of the SBM dynamics, and to run the Inertia Refiner algorithm. Both test and algorithm require some tuning to reach optimal results such as torque selection, acceleration time, sampling time and algorithm precision.

**Torque Selection** The torque applied to the assembly shall make more relevant the dynamical non-linearity, such as $J_{tot}w_{tot} \times w_{tot}$, while avoiding the non-linearity coming from the deformation of the mechanical link. A good compromise between these two characteristics has been found by considering a set of different torques in the same range of the one from the phase I of the system identification procedure, but simultaneously applied to each axe. Thus the torque chosen is $T = [1\ 2\ 3]^T\ Nm$.

**Acceleration Time** The acceleration time shall be chosen considering that non-linearity can arise over time during an acceleration, thus an increased acceleration time can allow for a more non-linear behaviour. On the other hand, longer acceleration time means a greater number of samples of angular velocity, accordingly to the sample time, which can result in either a stiffer problem to be solved by the algorithm or either a waste of time, if the samples are discarded because they are more than the required. Considering these factors, an acceleration time of 20 $s$ has been chosen for this test.

**Sample Time** The sample time of the angular velocity has to be chosen considering the Shannon-Nyquist theorem as lower limit, to avoid aliasing and loss of information, while the number of samples to collect is the upper limit. To respect the Shannon-Nyquist theorem, the knowledge of the maximum frequency of the angular velocity is required, unfortunately the maximum frequency is dependant on both velocity and inertia matrix at each time, thus calculating a precise frequency may not be convenient. Then sample frequency can be taken considering that during the acceleration, the system starts from a linear response, with zero max frequency, to a non-linear response, with a certain maximum frequency, meaning that the maximum frequency increases over time, and higher the angular velocity, higher the maximum frequency. Considering these evaluations, a value of 5 $Hz$ was considered as sampling frequency, hence a 0.2 $s$ sample time.

**Algorithm Precision** For the algorithm precision, the options of the constrained optimizer *fmincon* were set, together with the solver options for the propagation. For *fmincon* a number of $10^3$ maximum function evaluation and a step tolerance of $10^{-8}$ were consid-

ered, to increase the accuracy and to reduce the time required. For *ode45*, which is the solver to propagate the dynamics, a relative tolerance of $10^{-3}$ and an absolute tolerance of $10^{-6}$ were chosen. Moreover to speed up and improve the optimizer, the initial guess inertia matrix was rendered dimensionless.

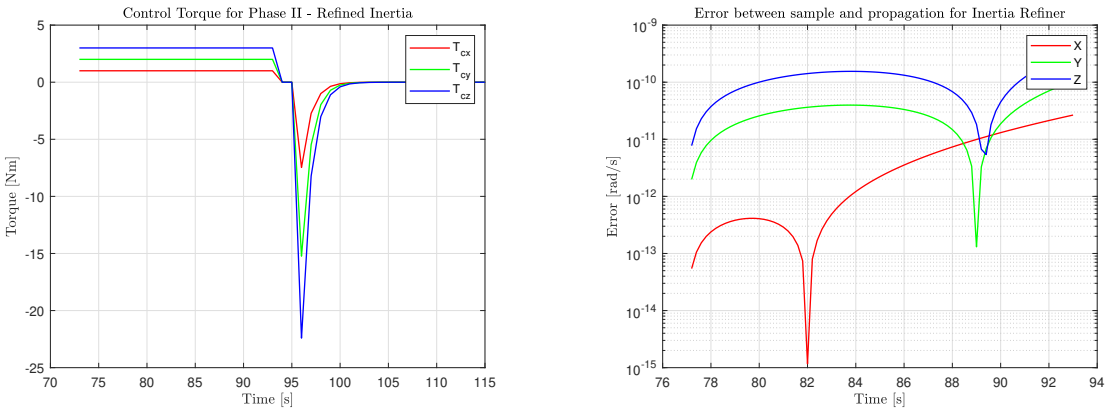


(a) Control torque over time

(b) Logarithmic error between sample and propagation

Figure 5.3: Control Torque and Algorithmic error for Phase II - Refined Inertia

To better analyze the outcome of this test, in Fig.5.3a the torque used to accelerate the system is shown, while in Fig.5.4 the angular velocity profile during the acceleration is presented for GEO case, since the differences in between GEO and MEO case are not significant. Moreover, to show the capabilities of the Inertia Refiner algorithm, in Fig.5.3b the logarithmic error between the sampled and propagated angular velocity is presented. The small logarithmic error suggests that the optimizer is able to fit the measured angular velocity profile, which underlines the dependency between the quality of the velocity profile given in input to the algorithm and the resulting error in estimation. Moreover, it can be seen that the logarithmic error for the z axis is some order of magnitude greater than the one of x axis, which is an expected behaviour.Two parallel effect have to be considered. In fact, the sloshing mass is positioned on the z-axis, and considering the dynamics, it receives more torque during the acceleration, which results in a higher angular velocity with respect to the other axis, since the diagonal terms of the inertia matrix are similar in order of magnitude. An higher angular velocity means an higher evolution rate for the dynamical system, which is directly related to the increase in error during a numerical propagation, which explains the difference in order of magnitude of the error.

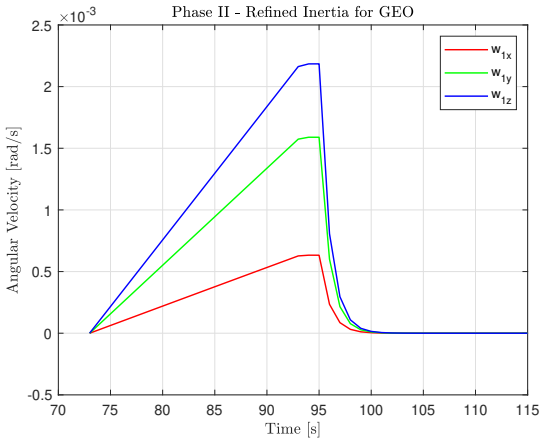


Figure 5.4: Angular velocity over time for Phase II - Refined Inertia

The final results of Phase II - Refined Inertia are presented in Tab.5.2. As in the previous Section, the error has been evaluated in three ways, plain error, diagonal error and extradiagonal error.

**Inertia Matrix results**

| | **Inertia Matrix** $[Kgm^2]$ | **Plain Difference** $[Kgm^2]$ | **Diagonal Error** $[Kgm^2]$ | **Extra-Diagonal Error** $[Kgm^2]$ |
|---|---|---|---|---|
| **Without Disturbances** | $\begin{bmatrix} 30142 & 327 & 249 \\ 327 & 25271 & -10 \\ 249 & -10 & 27711 \end{bmatrix}$ | $\begin{bmatrix} -0.055 & 0.12 & -0.01 \\ 0.12 & 0.47 & -0.37 \\ -0.01 & -0.37 & 0.3 \end{bmatrix}$ | 0.56 | 0.4 |
| **With GEO Disturbances** | $\begin{bmatrix} 30141 & 326 & 250 \\ 326 & 25271 & -9 \\ 250 & -9 & 27710 \end{bmatrix}$ | $\begin{bmatrix} 0.6128 & 1.27 & -1.06 \\ 1.27 & 0.37 & -1.30 \\ -1.06 & -1.30 & 1.15 \end{bmatrix}$ | 1.36 | 2.11 |
| **With MEO Disturbances** | $\begin{bmatrix} 30072 & 317 & 277 \\ 317 & 25276 & -12 \\ 277 & -12 & 27635 \end{bmatrix}$ | $\begin{bmatrix} 69.77 & 9.75 & -27.9 \\ 9.75 & -3.79 & 1.28 \\ -27.9 & 1.275 & 76.21 \end{bmatrix}$ | 103.4 | 29.53 |

Table 5.2: Results from Phase II - Refined Inertia

By comparing these results with the one in Tab.5.1, it is possible to assess the capability and utility of this algorithm. Considering the diagonal and extra-diagonal error, it can be

seen that the Inertia Refiner algorithm is capable to filter out the environmental disturbance affecting the spacecraft and to significantly improve the overall estimation of the inertia matrix.
On the other side, considering the plain difference error, it can be noticed that the error is more spread out between the single elements of the inertia matrix, meaning that the accuracy in estimation for the singular element may decrease after the refinement procedure. This is an effect produced by the nature of the algorithm, which considers the effects from the disturbing torque as part of the inertia matrix.

## 5.3. Phase III - Center of Mass

To estimate the position of the CM, two tests are required. The third phase shares not only the reasoning of linearity with the first phase of the system identification procedure, but also some parameters that impact the quality of the solution found, such as the thruster torque and the acceleration time.

**Thruster Torque** The torque by itself needs to be chosen by considering the limitation presented in Sec.5.1. As a matter of fact the controlling torque is required to be some orders of magnitude greater than the disturbing torques, making negligible their contribution to the final angular velocity, and at the same time a too intense torque may excite dynamical and visco-elastic non-linearity. For the thruster torque it is not possible to determine the relation between the torque and the force of the thruster without the knowledge of the CM, and some critical evaluations have to be made. If the detumbling process, which is executed by exchanging angular momentum with MED, is taken into consideration together with the notion that fuel is very precious and limited during the mission, the best choice for the thruster force is to select a small force if the thrusters are throttable, or either the smallest thruster force available from the ADCS engines. Two acceleration are required, and two force vector of $F_1 = [0.1\ 0\ 0]^T$ and $F_2 = [0\ 0.1\ 0]^T$ have been chosen for the first and second acceleration, respectively.

**Acceleration Time** The acceleration time choice follows closely the considerations stated in Sec.5.1, with an upper and lower limit. Considering the balance between controlling and disturbing torques, it is required to choose an acceleration time value that allows to consider the disturbing torque as negligible in determining the final angular velocity. As upper limit, it is necessary to consider that dynamical non-linearities may arise over time. Considering these upper and lower limits, a time of 10 $s$ has been chosen for acceleration time for each acceleration.

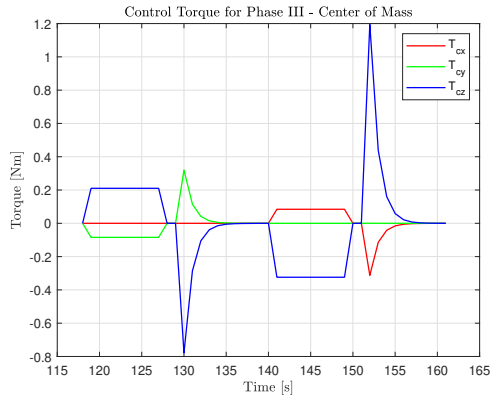


Figure 5.5: Control torque over time for Phase III - Center of Mass

To properly evaluate the outcome of the tests procedure, the angular velocities for GEO and MEO cases are shown in Fig.5.6. Since the torque behaviour during these tests is not known beforehand, a plot of its profile is presented in Fig.5.5.
It is important to notice the linearity between angular velocity and controlling torque, since two torques are applied simultaneously in each test, meaning that the gyroscopic term inside the EoM is small enough to be negligible and validating the reasoning of Sec.4.3.1.
Comparing Fig.5.6 with Fig.5.2 for the MEO case, it is possible to ascertain the reduced impact of the disturbing torque due to the fact that the spacecraft uses a detumbling control law during the braking phases, with the refined inertia matrix as control gain. This allows the assembly to reach zero angular velocity and avoid the buildup error phenomena that impacts the estimation accuracy of the coarse inertia matrix.

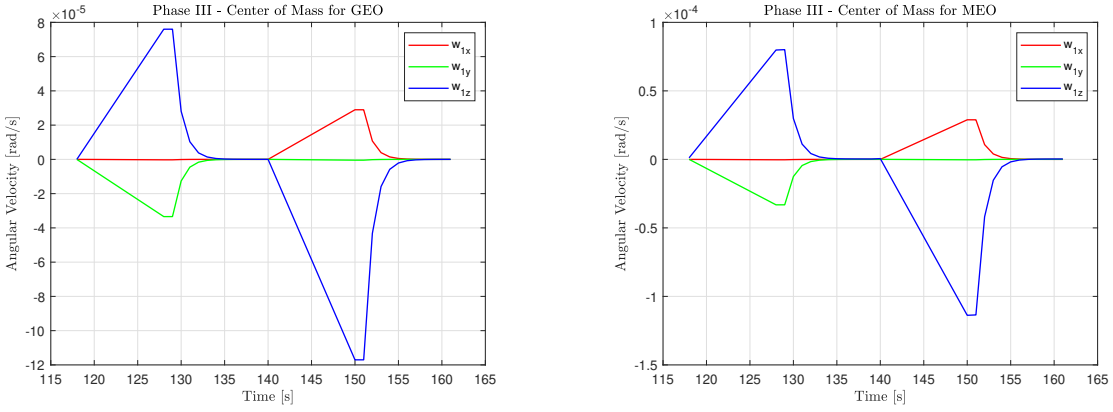


(a) GEO case (b) MEO case

Figure 5.6: Angular velocity over time for Phase III - Center of Mass

The final results from Phase III - Center of Mass are presented in Tab.5.3. Results are presented considering the final value outcome, the plain error between the resulting value and the original value, as norm of the error vector, and lastly by relative error as fraction between the error and the norm of the original value. While considering these results, it

is important to keep in mind that the precision of the final value is also determined by the precision of the inertia matrix $J_{tot}$ calulated by the previous tests.

**Center of Mass results**

| | **Center of Mass** $[m]$ | **Plain Error** $[m]$ | **Absolute Error** $[m]$ | **Relative Error** $[-]$ |
|---|---|---|---|---|
| **Without Disturbances** | $[1.74\ 0.35\ -0.35]^T$ | $[-0.008\ 0.001\ 0.01]^T$ | 0.01 | 2.9% |
| **With GEO Disturbances** | $[1.74\ 0.36\ -0.36]^T$ | $[0.003\ -0.002\ 0.009]^T$ | 0.01 | 2.7% |
| **With MEO Disturbances** | $[1.64\ 0.46\ -0.36]^T$ | $[0.1\ -0.1\ 0.01]^T$ | 0.14 | 29.6% |

Table 5.3: Results from Simple tests - Center of Mass

Comparing the results in estimation of the center of mass position it can be noted that the error does not increase between the without disturbance and the GEO cases, while between the GEO and MEO cases the accuracy decreases as the environmental disturbances increase. The loss of CM position accuracy is not only connected to the increase in disturbance torques, but can be mainly linked to the accuracy of the inertia matrix estimation and not due to the increase interference from the disturbances. This relation can be explained taking into consideration the angular velocity in Fig.5.6, where a very similar angular velocity is reached at the end of the acceleration, meaning that the loss in accuracy is only partially linked to the acting disturbances during the test.

## 5.4. Phase IV - Docked spacecrafts properties

The fourth phase of the system identification procedure is a mathematical one, since only the values $J_{1cm}$ and $J_{2cm}$ are being evaluated, and are results of the estimation of the inertia matrix and CM position. In Tab.5.4 and in Tab.5.5 the results for $J_{1cm}$ and $J_{2cm}$ are presented, respectively.

**Inertia Matrix results for first body**

| | **Inertia Matrix** $[Kgm^2]$ | **Plain Difference** $[Kgm^2]$ | **Diagonal Error** $[Kgm^2]$ | **Extra-Diagonal Error** $[Kgm^2]$ |
|---|---|---|---|---|
| **Without Disturbances** | $\begin{bmatrix} 15369 & 136 & 122 \\ 136 & 6536 & -6 \\ 122 & -6 & 19410 \end{bmatrix}$ | $\begin{bmatrix} -2.6 & -3.8 & -28.8 \\ -3.8 & -7 & 1.2 \\ -28.8 & 1.2 & -5 \end{bmatrix}$ | 9 | 29 |
| **With GEO Disturbances** | $\begin{bmatrix} 15360 & 126 & 119 \\ 126 & 6515 & -5.6 \\ 119 & -5.6 & 19390 \end{bmatrix}$ | $\begin{bmatrix} -1.7 & 6.4 & -25.8 \\ 6.4 & 13.8 & 0.7 \\ -25.8 & 0.7 & 16.32 \end{bmatrix}$ | 21.4 | 26.6 |
| **With MEO Disturbances** | $\begin{bmatrix} 15360 & -147 & 121 \\ -147 & 5970 & 7.8 \\ 121 & 7.8 & 18840 \end{bmatrix}$ | $\begin{bmatrix} -5.9 & 280 & -28 \\ 280 & 560 & -12.7 \\ -28 & -12.7 & 560 \end{bmatrix}$ | 792 | 281.3 |

Table 5.4: Estimation of the inertia matrix $J_{1cm}$

**Inertia Matrix results for second body**

| | **Inertia Matrix** $[Kgm^2]$ | **Plain Difference** $[Kgm^2]$ | **Diagonal Error** $[Kgm^2]$ | **Extra-Diagonal Error** $[Kgm^2]$ |
|---|---|---|---|---|
| **Without Disturbances** | $\begin{bmatrix} 14780 & 191 & 127 \\ 191 & 18730 & -4 \\ 127 & -4 & 8303 \end{bmatrix}$ | $\begin{bmatrix} 2.6 & 3.9 & 28.7 \\ 3.9 & 7.5 & -1.6 \\ 28.7 & -1.6 & 5.3 \end{bmatrix}$ | 9.5 | 29 |
| **With GEO Disturbances** | $\begin{bmatrix} 14780 & 200 & 131.2 \\ 200 & 18760 & -3.8 \\ 131 & -3.8 & 8324 \end{bmatrix}$ | $\begin{bmatrix} 2.3 & -5.1 & 24.7 \\ -5.1 & -13.4 & -2 \\ 24.7 & -2 & -15 \end{bmatrix}$ | 20.35 | 25.35 |
| **With MEO Disturbances** | $\begin{bmatrix} 14710 & 465 & 156 \\ 465 & 19310 & -19.8 \\ 156 & -19.8 & 8793 \end{bmatrix}$ | $\begin{bmatrix} 75.7 & -270 & -0.12 \\ -270 & -563 & 14 \\ -0.12 & 14 & -485 \end{bmatrix}$ | 747 | 270 |

Table 5.5: Estimation of the inertia matrix $J_{2cm}$

It is interesting to note that the error in each inertia matrix is higher than the estimation of

the whole inertia matrix, and moreover, the error shows a symmetrical behaviour between $J_{1cm}$ and $J_{2cm}$. Both effects are caused by the estimation of the position of the CM, which shows the great impact in accuracy of estimation for each case. As expected, the error increases with the presence of environmental disturbance torque, following the trend of the inertia matrix and the center of mass.
The properties of the second satellite are not here reported, as discussed in Sec.4.4.2. As a matter of fact, the measure of the total mass would be always perfect, and thus the final results on the identification of the second body would only depend on the estimation of the inertia matrix and CM position of the whole Assembly, as $J_{1cm}$ and $J_{2cm}$ are.

## 5.5. Phase V - Visco-Elastic Fitting

The estimation of the visco-elastic coefficients requires a single test that makes use of the non-linearities coming from both dynamics and the visco-elastic mechanical link between the two satellites. Similarly to Sec.5.2, torque, acceleration time, sample time and algorithm precision are parameters to that can be tuned to reach optimal results.

**Torque** To select a proper torque, it is necessary to consider that both dynamical non-linearities, such as $J_{1cm}\dot{\theta}_1 \times \dot{\theta}_1$ and $J_{2cm}\dot{\theta}_2 \times \dot{\theta}_2$, and visco-elastic non-linearities, $K(\theta_1 - \theta_2)$ and $C(\dot{\theta}_1 - \dot{\theta}_2)$ , have to become more relevant inside the EoM. Considering the algorithm and the propagation inside the optimizer, a great torque results in a reduction of the precision of the propagation and an increase of the computational burden. Moreover the limits in torque output from actuators have to be taken into account. To respect these characteristics, a set of different torques simultaneously applied to each axe in a range higher than the one used in the previous tests was considered. The final choice for the torque is $T = [10\ 20\ 30]\ Nm$.

**Acceleration Time** To choose the acceleration time, it is important to consider that dynamical non-linearity may arise over time, while the visco-elastic ones are more relevant at the beginning of the acceleration, and may decrease if the acceleration is constant. Moreover, the acceleration time regulates the number of samples taken, if the sample time is set. This may result in an excessive or reduced sample size, which may impact the performance and results of the algorithm, or may result in a waste of time if the excess samples are discarded. Given these factors, an acceleration time of 10 $s$ was chosen.

**Sample Time** The sample time of the angular velocity has to be chosen considering the Shannon-Nyquist theorem, to avoid aliasing and loss of information, and the number

of samples to collect is the upper limit. The Shannon-Nyquist theorem requires the knowledge of the maximum frequency of the angular velocity oscillations. This maximum frequency is dependant on both the gyroscopic term and the visco-elastic properties of the mechanical link. Calculating a precise frequency may not be convenient since the oscillations coming from the visco-elastic components are dependant from $K$ and $C$, which are yet to be found. A consideration can be made, from the conditions given by the problem. If the values of $K$ are in a neighborhood of three orders of magnitude around the values of $J_{tot}$ and recalling the equation of the proper frequency:

$$w_n = \sqrt{\frac{K}{J_{tot}}} \tag{5.1}$$

Where $w_n$ is the natural frequency, the ratio $\frac{K}{J}$ shall be around $10^2\ Hz$, meaning that the natural frequency shall less than $10^1\ Hz$. Considering these evaluations, a value of 10 Hz was considered as sampling frequency, hence a 0.1 s sample time.

**Algorithm Precision** To set the algorithm precision, both options for the non-linear least-squares curve fitting *lsqnonlin* and the solver to propagate the system *ode45* are set. For *lsqnonlin* the number of maximum function evaluations has been set as $10^3$, the step tolerance of $10^{-5}$, optimality tolerace of $10^{-14}$, function tolerance of $10^{-10}$ and a number of maximum iterations of 30, which help increase the precision and reduce computational time. For *ode45* a relative tolerance of $10^{-3}$ and an absolute tolerance of $10^{-6}$ have been set. To speed up and improve the optimizer, the initial guess was taken as the major value inside $J_{tot}$ which was rendered dimensionless.

To better analyze the outcome of this test, in Fig.5.7a the Torque used to accelerate the system during the test is shown, while in Fig.5.8 the angular velocity profile during the acceleration is presented for GEO cases, since the difference between GEO and MEO are not significant. Moreover, to show the capabilities of the Visco-Elastic Fitter algorithm, in Fig.5.7b the logarithmic error between the sampled and propagated angular velocity is presented.

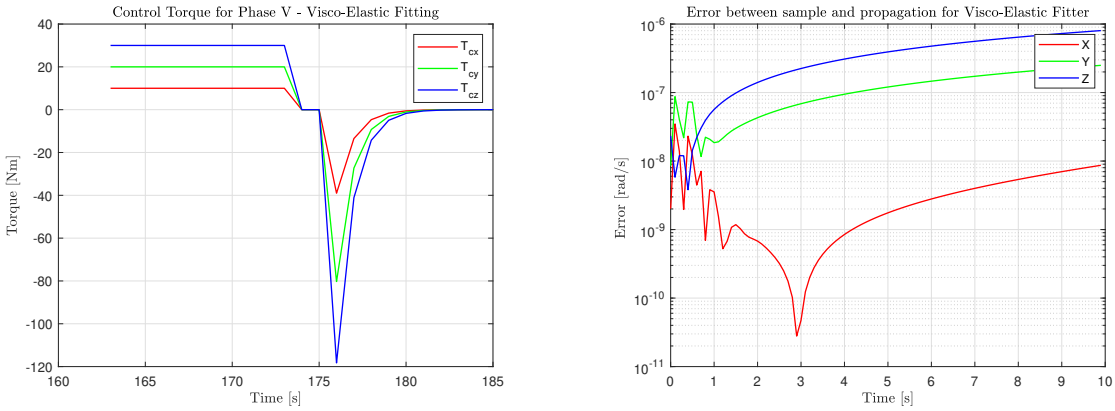


(a) Control torque over time

(b) Logarithmic error between sample and propagation

Figure 5.7: Control Torque and Algorithmic Error for Phase V - Visco-Elastic Fitting

Considering the logarithmic error, it can be verified that the algorithm is able to fit the angular velocity profile in input. Specifically it can be seen that the error at the beginning of the profile is noisy, which suggests the predominance of visco-elastic effects which are associated with the beginning of the step input torque. The error then smooths out during the rest of the propagation since the input torque is constant. As in the Inertia Refiner algorithm, the logarithmic error is greater on z component which is related to the presence of the sloshing mass, together with the greater torque applied and higher velocity reached, factors that increase the propagation error.

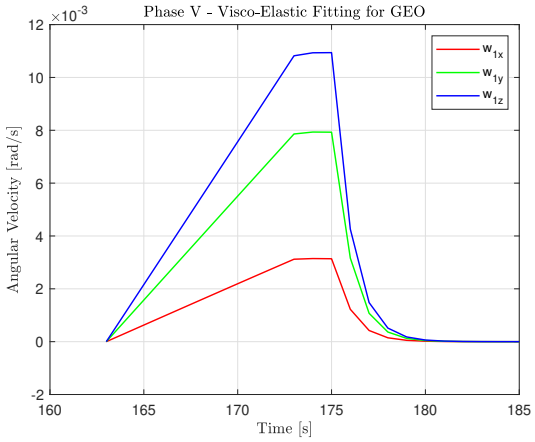


Figure 5.8: Angular velocity over time for Phase V - Visco-Elastic Fitting

The final results of fifth phase of the system identification procedure are presented in Tab.5.6 and in Tab.5.7 for the elastic and viscous coefficients respectively. The error has

been evaluated as: plain error between the resulting value and the original value, norm of the error vector, and lastly by relative error as fraction between the error and the norm of the original values for each coefficient, $K$ and $C$. It is important to point out that the overall results are directly influenced by the results from the previous tests.

**Elastic coefficient**

| | **Final Value** | **Plain Error** | **Absolute Error** | **Relative Error** |
|---|---|---|---|---|
| **Without Disturbances** | $10^6[1.2\ 0.7\ 0.9]$ | $10^3[10.4\ 2.4\ 2.6]$ | $1.1\ 10^4$ | 0.98% |
| **With GEO Disturbances** | $10^6[1.2\ 0.7\ 0.85]$ | $10^3[6.5\ -0.4\ -1.77]$ | $6.7\ 10^3$ | 0.6% |
| **With MEO Disturbances** | $10^6[1.3\ 0.7\ 0.9]$ | $10^4[-4.8\ -1.7\ -7.9]$ | $9.4\ 10^4$ | 10.4% |

Table 5.6: Elastic coefficient from Phase V - Visco-Elastic Fitting

**Viscous coefficient**

| | **Final Value** | **Plain Error** | **Absolute Error** | **Relative Error** |
|---|---|---|---|---|
| **Without Disturbances** | $10^5[0.9\ 0.8\ 1.1]$ | $10^2[5.6\ 4.2\ 10.6]$ | 1268 | 1.26% |
| **With GEO Disturbances** | $10^5[0.9\ 0.8\ 1.09]$ | $10^2[4.3\ -1.2\ 0.9]$ | $4.5\ 10^2$ | 0.5% |
| **With MEO Disturbances** | $10^5[1\ 0.86\ 1.17]$ | $10^3[-9.7\ -5.5\ -7.2]$ | $1.33\ 10^4$ | 14.4% |

Table 5.7: Viscous coefficient from Phase V - Visco-Elastic Fitting

Comparing the two tables of results for the estimation of the visco-elastic coefficients, it can be seen that both values are estimated with a similar accuracy in different condition of environmental disturbance, meaning that the algorithm makes no preference during the optimization. Moreover it is possible to see that the accuracy decreases with a significant leap between the GEO and MEO cases. This effect has its origin in the increase in disturbance torque which impacts not only the angular velocity profile, but also the

estimation of the inertia matrices of each body, $J_{1cm}$ and $J_{2cm}$, which is strongly related to the estimation of both $J_{tot}$ and the CM position, leading to a buildup in error.
Strangely, a small improvement of the accuracy can be observed comparing the without disturbance case and the GEO case. This phenomena can possibly be correlated with the numerical optimization iteration, which convergence may be improved by using different input data.

## 5.6. Sensibility Analysis

To understand the robustness and the limits of the system identification procedure, a series of sensitivity analysis test have been carried out. This allows to identify the relationships between the uncertainties expected in real-life scenarios with the results obtained, and identify the sources of error.

### 5.6.1. Torque Delivery Mismatch

To evaluate the sensitivity of the system identification procedure to the mismatch in torque delivery, such phenomena has been simulated considering a range of ±5% on the torque delivered. In this case, the relative error has been considered as evaluation parameter and is shown in Fig.5.9 as function of torque mismatch.

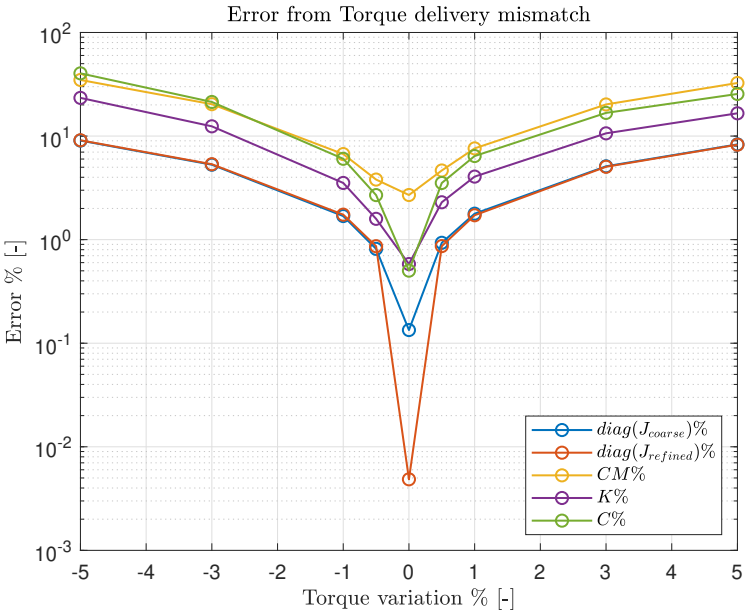


Figure 5.9: Percentage Error as function of torque delivery mismatch

The system identification procedure is heavily impacted by torque delivery mismatch,

specifically above ±0.5% the error increases significantly, remarking the strong relation between the torque delivery precision and the accuracy of the results. It can be seen that the torque delivery mismatch significantly affects all the results in a symmetrical fashion from the zero, since the error is built up from the inertia matrix estimation to the visco-elastic coefficients. Interestingly the percentage error of the diagonal elements of the inertia matrix increases in the same way for both the coarse and refined estimations, this can be traced back to the fact that the coarse inertia matrix is used as initial guess for the Inertia Refiner algorithm, and that the objective for such algorithm is to filter out disturbances that are much lower than the torque mismatch taken in consideration.

### 5.6.2. Force Delivery Mismatch

The force delivered by the thrusters is crucial in determining the position of the CM. To evaluate the sensibility of the algorithm, a percentage error of ±5% of the thruster force has been considered. The relative error has been considered as parameter evaluation and its behaviour is presented in Fig.5.10.

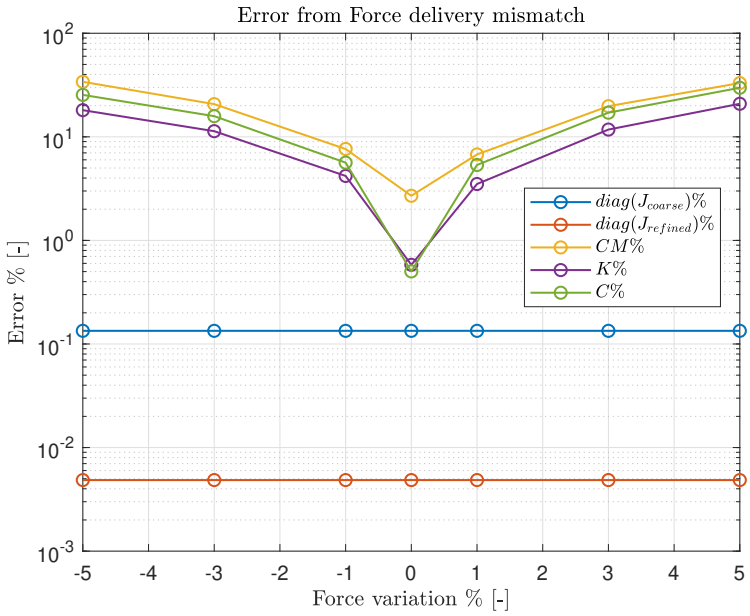


Figure 5.10: Percentage Error as function of torque delivery mismatch

As expected, the error in estimation of the inertia matrix is independent from the thruster force, while the CM error behaves symmetrically from the zero. It is interesting to notice that the behaviour of both $K$ and $C$ error changes together with the CM one, even if no mismatch in torque magnitude is present during the angular velocity sampling. In this case the error can be traced back to the determination of $J_{1cm}$ and $J_{2cm}$, which relies on

the position of the CM, and are crucial values for the Double Body Model propagation.

### 5.6.3. Torque Misalignment

As part of the sensibility analysis, the torque misalignment phenomena has been considered, which may occur due to installation, ageing and wearing out of the mechanical and/or electrical parts. If the exact alignment of the axis is not accurate, large errors in output torques may impact the attitude of the spacecraft[30]. To simulate the effects of a misaligned torque, the misalignment model for a set of three reaction wheels has been taken into consideration [4, 10], since it allows to directly control the misalignment by using deviation angles.
To define the impact of the misalignment on the system identification performance, a Montecarlo Analysis has been carried out. Considering that previous launched missions have not surpassed 7° [28] in actuator angular misalignment, and that it is important to study the behaviour around the zero angular misalignment, 100 set of 3 deviation angles have been generated considering a normal distribution with zero mean, and a variance of 1°. The results of the Montecarlo analysis are reported in Fig.5.11 in terms of relative error over the norm of the deviation angles.


Figure 5.11: Montecarlo analysis for torque misalignment

It is interesting to notice that the results for the coarse estimation of the inertia matrix does not suffer from the increase in angular deviation of the torque and provides a better estimation than the refined one. The accuracy behaviour of the refined inertia matrix

is shared with the estimation of $K$ and $C$, for two main reasons: both estimations are performed by using numerical methods and have uneven accelerating torque with greater magnitude on the Z-axis, which creates a significant difference between samples with similar norm of the deviation angles. The accuracy for CM estimation follows the one of the refined inertia matrix, being its direct result, but similarly to the coarse estimation of the inertia matrix, it is less dependant from the torque misalignment.
As final note, considering together Fig.5.10 and Fig.5.11, the sensibility of the refined inertia matrix regarding torque accuracy can be assessed: if the knowledge accuracy of the torque is insufficient, the refined inertia matrix is not able to provide a better estimation than the coarse one.

### 5.6.4. Force Misalignment

The last step to perform a correct sensitivity analysis related to poor actuator knowledge is to consider the misalignment phenomena regarding the thruster force. To simulate the misalignment of the thruster force, rotation matrix have been developed to take into account the deviation angles as used in [29, 31]. Similarly to the torque misalignment sensitivity analysis, a Montecarlo analysis has been carried out. The misalignment angles were generated by considering a normal distribution with zero mean and 1° variance, which can be considered reasonable since the objective of the analysis is to study the behaviour around the zero deviation angle. The results for the Montecarlo analysis are presented in Fig.5.12 in terms of relative error over norm of the deviation angles.

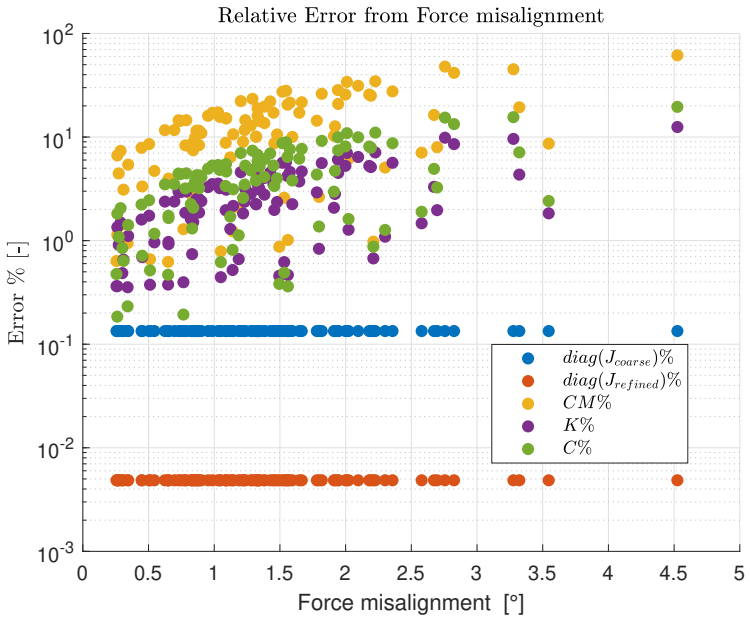


Figure 5.12: Montecarlo analysis for force misalignment

As in Fig.5.10, the results from coarse and refined estimation of the inertia matrix are not influenced by the misalignment of the thruster force, while the estimation error for CM position increases with a linear pattern with the angular deviation. As expected, the estimation error of $K$ and $C$ coefficients increases in a similar fashion as the one of CM position, which is used to evaluate $J_{1cm}$ and $J_{2cm}$. On the other side it is interesting to notice that the $K$ and $C$ relative error increase is not as steep as the one of the CM, meaning that the Visco-Elastic Fitter algorithm is capable of filtering out not only uncertainties coming from the external environment, but also inaccurate data.

### 5.6.5. Angular velocity sensibility analysis

The measure of the angular velocity is crucial for the outcome of the system identification procedure, being required for each estimation. Hence a sensitivity analysis has been carried out considering two main factors that may affect the measure of the angular velocity: offset error and noise error.

**Angular velocity offset error** Offset error has been simulated considering a steady source of error to be added to the angular velocity measure. Considering the angular velocity reached during the estimation process, a set of constant angular velocity error in the range between $10^{-4}$ $\frac{rad}{s}$ and $10^{-8}$ $\frac{rad}{s}$ has been used for the sensitivity analysis. The results from offset error are shown in Fig.5.13 in terms of relative error.

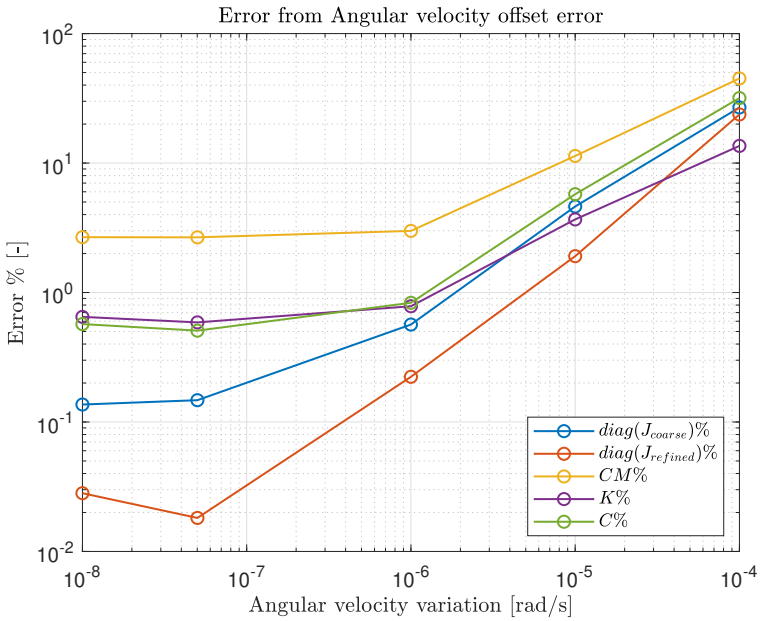


Figure 5.13: Offset angular velocity error

It can be seen that the relative error changes in a similar fashion with the increase of the offset error for each estimation. In particular, a threshold can be identified at $10^{-6}\frac{rad}{s}$, since the estimation does not improve significantly for smaller values of offset error, while the error increases above the threshold. This phenomena can be addressed to the fact that values of offset error greater than $10^{-6}\frac{rad}{s}$ are in the similar order of magnitude with the actual angular velocity reached during the estimation process, while smaller values can be treated as effects from disturbances.

**Angular velocity noise error** The noise error that may affect the angular velocity has been emulated by considering a random source of error which is added to the angular velocity measure. The random source has been identified as a normal distribution with zero mean, while a set of variances in the range between $10^{-4}$ $\frac{rad}{s}$ and $10^{-8}$ $\frac{rad}{s}$ have been considered to simulate different order of noise intensity. The results in terms of relative error over the angular velocity noise error are presented in Fig.5.14.

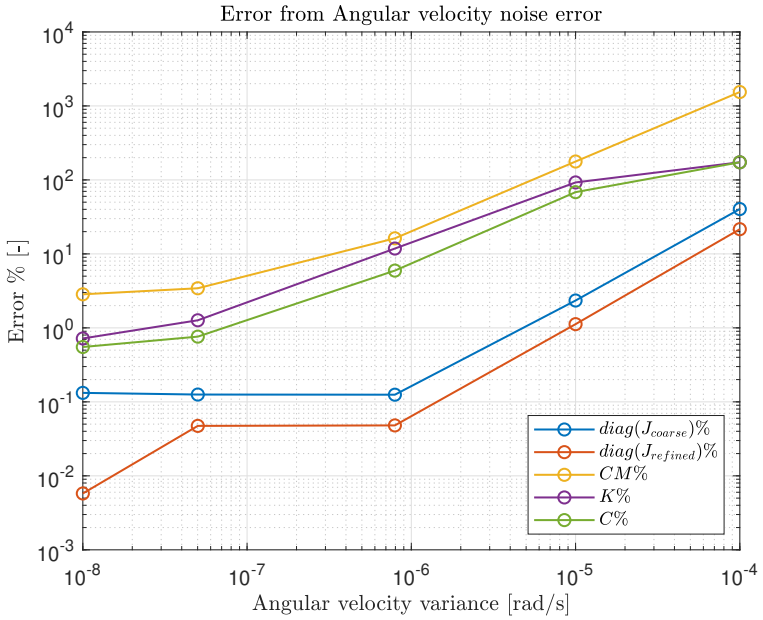


Figure 5.14: Angular velocity noise error

This image presents some similarities with Fig.5.13, as a matter of fact a threshold on $10^{-6}$ $\frac{rad}{s}$ can be noticed, especially on the estimation of the inertia matrix. It can be seen that for smaller variance values than the threshold, the coarse and refined estimations of the inertia matrix do not improve significantly, meaning that the noise level is similar to the effects on the angular velocity from the environmental disturbances, while for greater variance values the relative error increases linearly. The estimation error of the

visco-elastic coefficients and the CM on the other hand reduces linearly together with the orders of magnitude of the variance up to $10^{-7}$ $\frac{rad}{s}$, after which the improvement of the relative error is reduced.
Comparing Fig.5.13 and Fig.5.14, it is possible to assess the sensitivity of the system identification procedure, and to acknowledge the noise error as more relevant than the offset error for the accuracy of the results.

# 6 | Chapter 6 - Control Performance Comparison

In this chapter the control performance assessment of the results found in Ch.5 is presented. To assess the utilty of the new data available from the system identification procedure, a set of control tests have been considered. The control tests are focused on verifying and comparing the pointing accuracy of the whole Assembly in two cases: Before System Identification Procedure (BSIP) and After System Identification Procedure (ASIP). In the first section the control laws and the rationale behind them are presented, while in the second section the results and comparison are presented.

## 6.1. Control Modes and Control Laws

To assess the capabilities of the satellite assembly before and after the system identification procedure, three control modes have been considered for the control tests: inertial pointing, repointing and tracking. Before going through each control mode, the reachability and observability of the system have been verified to implement a feedback control.

### 6.1.1. Feedback Control

To assess the possibility of implementing a Feedback Control for the whole Assembly, firstly the reachability and observability of the dynamical system has to be assessed.

The EoM of the DBM, which is Eq.3.4, can be rewritten as a state-space system:

$$\begin{cases} \begin{bmatrix} \ddot{\theta}_1 \\ \dot{\theta}_1 \\ \ddot{\theta}_2 \\ \dot{\theta}_2 \end{bmatrix} = \begin{bmatrix} -J_{1cm}^{-1}C & -J_{1cm}^{-1}K & J_{1cm}^{-1}C & J_{1cm}^{-1}K \\ 1 & 0 & 0 & 0 \\ J_{2cm}^{-1}C & J_{2cm}^{-1}K & -J_{2cm}^{-1}C & -J_{2cm}^{-1}K \\ 0 & 0 & 1 & 0 \end{bmatrix} \begin{bmatrix} \dot{\theta}_1 \\ \theta_1 \\ \dot{\theta}_2 \\ \theta_2 \end{bmatrix} + \begin{bmatrix} J_{1cm}^{-1} \\ 0 \\ J_{2cm}^{-1} \\ 0 \end{bmatrix} u \\ y = \begin{bmatrix} 1 & 1 & 0 & 0 \end{bmatrix} \begin{bmatrix} \dot{\theta}_1 \\ \theta_1 \\ \dot{\theta}_2 \\ \theta_2 \end{bmatrix} \end{cases} \tag{6.1}$$

Which can be shortened in:

$$\begin{cases} \dot{x} = A_{lin}x + B_{lin}u \\ y = C_{lin}x \end{cases} \tag{6.2}$$

In which $A_{lin}$ is the matrix of dynamic, $B_{lin}$ is the feed-through matrix and $C_{lin}$ is the output matrix.

**Reachability** The reachability of a dynamical system refers to the capability of the system to reach every possible state from any initial state in a finite amount of time, moreover a dynamical system is said to be reachable if the reachability matrix is full rank:

$$R_r = [B_{lin}\ A_{lin}B_{lin}\ A_{lin}^2B_{lin}\ A_{lin}^3B_{lin}] \tag{6.3}$$

In this case, the rank of the reachability matrix $R_r$ is 4, meaning that the system is indeed reachable.

**Observability** The observability of a dynamical system refers to the capability of reconstructing the state of the system from a time-finite output of the system, specifically a dynamical system is said to be reachable if the observabilty matrix is full rank:

$$Oss_r = \begin{bmatrix} C_{lin} \\ C_{lin}A_{lin} \\ C_{lin}A_{lin}^2 \\ C_{lin}A_{lin}^2 \end{bmatrix} \tag{6.4}$$

In this case, the rank of the observability matrix $Oss_r$ is 4, meaning that the system is indeed observable.

Being the system both reachable and observable, implies the possibility to control the state of the system, and to observe the state reached. This means that a feedback control can be implemented as control law.

### 6.1.2. Inertial Pointing

The first control mode considered is the inertial pointing mode. The inertial pointing mode requires the spacecraft to follow a certain angular velocity profile over time. This control mode can be used either to point an inertial target, requiring stillness of the spacecraft, or either to point a target with known velocity profile, for example a point on the surface of the Earth during a transit of the spacecraft.
Considering simple feedback control laws, and the available data from sensors, the family of Proportional Integrative Derivative (PID) control has been considered, specifically a Proportional control based on the angular velocity of the first satellite:

$$T_c = -K_p w_e + w_1 \times J w_1 \tag{6.5}$$

Where $T_c$ is the control torque, $J$ is the inertia matrix, $J_1$ for BSIP and $J_{tot}$ for ASIP cases, $K_p$ is the gain for the proportional action and $w_e$ is the angular velocity error:

$$w_e = w_{obj} - w_1 \tag{6.6}$$

In which $w_{obj}$ is the target angular velocity and $w_1$ is the angular velocity of the first satellite.
The angular velocity of the first satellite was chosen as control parameter since it is a measurement available for both BSIP and ASIP cases, while the gain parameters were set individually for each case.
For the BSIP case, the gain coefficient is equal to $J_1$, which is the inertia matrix of the first satellite centered on the CM of the first satellite, in this way the first satellite controls the whole Assembly as if only the first satellite were present. For the ASIP case, the proportional coefficient is equal to $J_{tot}$, which is the inertia matrix centered on the CM of the whole Assembly, allowing the first satellite to control the system as a whole spacecraft. For this control mode the inertia matrices were used as gains since they can make the control torque proportional to the order of magnitude of the dynamical system, which is regulated by the inertia matrix itself.

### 6.1.3. Repointing

The second control mode considered is the repointing mode. In the repointing mode, the spacecraft executes a slew manoeuvre, which is a rest-to rest motion between two different attitude, and sets its attitude to point a certain target. In this case the chosen target is the Sun, which would allow the spacecraft to recharge its batteries in an hypothetical real mission scenario.
Considering simple feedback control laws, the classical control function for repointing were considered, specifically the quaternion feedback control, while the gain coefficient for each term has been treated as a Proportional Integrative (PI) control. Such control law is defined in [27], and takes into consideration the quaternion error and the angular velocity of the first body:

$$T_c = -K_i q_e - K_p w_1 + w_1 \times J w_1 \tag{6.7}$$

In which $q_e$ is the quaternion error:

$$\begin{bmatrix} q_{1e} \\ q_{2e} \\ q_{3e} \\ q_{4e} \end{bmatrix} = \begin{bmatrix} q_{4c} & q_{3c} & -q_{2c} & -q_{1c} \\ -q_{3c} & q_{4c} & q_{1c} & -q_{2c} \\ q_{2c} & -q_{1c} & q_{4c} & -q_{3c} \\ q_{1c} & q_{2c} & q_{3c} & q_{4c} \end{bmatrix} \begin{bmatrix} q_1 \\ q_2 \\ q_3 \\ q_4 \end{bmatrix} \tag{6.8}$$

Specifically $q_e = [q_{1e}\ q_{2e}\ q_{3e}]^T$ is used inside Eq.6.7, while $q_c$ are the objective quaternions, which are obtained from the conversion of the target attitude matrix into quaternion representation. The target attitude matrix $A_{S/N}$ is considered taking in consideration the direction of the Sun in the inertial frame $S_N$ as x-axis, while for the y and z axis are simply required to be linearly independent between each other. Then a generic direction is taken, $p = [1\ 0\ 0]$ and the target attitude can be generated:

$$\begin{cases} s_1 = S_N \\ s_2 = \frac{s_1 \times p}{|s_1 \times p|} \\ s_3 = s_1 \times s_2 \end{cases} \qquad A_{S/N} = \begin{bmatrix} s1 \\ s2 \\ s3 \end{bmatrix} \tag{6.9}$$

The term $w_1 \times J w_1$ inside Eq.6.7, counters the gyroscopic term inside the Eq.3.1.
The angular velocity, together with the attitude of the first satellite were chosen as control parameters since both measurements are available for both BSIP and ASIP cases.
While simulating the BSIP case, the gain coefficients $K_i$ and $K_p$ were set equal to $J_1$, meaning only with the knowledge of the inertial data of the first satellite. For the the ASIP case, some adjustments have been made, and a slew rate limit has been introduced.

**Slew rate limit** A classical slew manoeuvre is divided in three phases, acceleration, coasting and deceleration. Considering the coasting phase, the slew rate, thus the angular velocity, is constant, and acceleration is zero. Under these considerations both angular velocity ($\dot{\theta}_2$ and $\dot{\theta}_1$) are equal, and the term $C(\dot{\theta}_2 - \dot{\theta}_1)$ can be considered negligible, then it is possible to write Eq.3.4 in this form:

$$\begin{cases} 0 = J_{1cm}\dot{\theta}_1 \times \dot{\theta}_1 + K(\theta_2 - \theta_1) + M_{ext} \\ 0 = J_{2cm}\dot{\theta}_2 \times \dot{\theta}_2 + K(\theta_1 - \theta_2) \end{cases} \tag{6.10}$$

Which implies the relation:

$$K(\theta_2 - \theta_1) = J_{2cm}\dot{\theta}_2 \times \dot{\theta}_2 \tag{6.11}$$

This means that the angular difference between the first and the second satellite during a slew motion is directly influenced by the slew rate, thus limiting the slew rate limits the angular difference. To develop a slew rate limit, it is fundamental to identify a maximum angular velocity. Even if the maximum angular difference is set, due to the presence of the cross product, Eq.6.11 has no single solution, and two different workaround can be made. A first workaround would be to check Eq.6.11 continuously during the motion, and put a deactivation condition on to the torque:

$$\begin{cases} T_c = -K_i q_e - K_p w_1 + w_1 \times J w_1 \\ T_c = w_1 \times J w_1 \end{cases} \quad if \begin{cases} J_{2cm}\dot{\theta}_1 \times \dot{\theta}_1 < K\Delta\theta_{max} \\ J_{2cm}\dot{\theta}_1 \times \dot{\theta}_1 >= K\Delta\theta_{max} \end{cases} \tag{6.12}$$

Where $\Delta\theta_{max}$ is the maximum angular difference. This workaround is inefficient since it can slow down the computation due to the trigger *if condition*, which can affect the smoothness of the motion.
A second workaround can be made considering the properties of the eigen axis angular rotation:

$$\Delta\theta_{max} = \begin{bmatrix} e_1 \\ e_2 \\ e_3 \end{bmatrix} ||\Delta\theta_{max}|| \; and \; w = \begin{bmatrix} e_1 \\ e_2 \\ e_3 \end{bmatrix} ||w|| \tag{6.13}$$

Where $e_1$, $e_2$ and $e_3$ compose the Euler axis of rotation, while $w$ is the generic angular velocity. The components of the Euler axis of rotation can be put into relation with the quaternion error vector at the beginning of the slew manoeuvre $q_e(0)$:

$$e_1 = \frac{|q_{1e}(0)|}{||q_e(0)||} \; e_2 = \frac{|q_{2e}(0)|}{||q_e(0)||} \; e_3 = \frac{|q_{3e}(0)|}{||q_e(0)||} \tag{6.14}$$

It is now possible to rewrite Eq.6.11 and put into relation $\dot{\theta}_{max}$, which is the maximum slew rate during the manoeuvre with $\Delta\theta_{max}$:

$$||\dot{\theta}_{max}||^2 = (J_{2cm} \begin{bmatrix} e_1 \\ e_2 \\ e_3 \end{bmatrix} \times \begin{bmatrix} e_1 \\ e_2 \\ e_3 \end{bmatrix})^{-1} K \begin{bmatrix} e_1 \\ e_2 \\ e_3 \end{bmatrix} ||\Delta\theta_{max}|| \tag{6.15}$$

Once the maximum slew rate is known, the control gains of Eq.6.7 can be defined :

$$K_p = J_{tot} \ and \ K_i = J_{tot} \frac{|q_{ie}(0)|}{||q_e(0)||} ||\dot{\theta}_{max}|| \tag{6.16}$$

This procedure allows for smooth control during the slew manoeuvre and a limited computational burden, since Eq.6.15 is evaluated one single time.
Once the slew manoeuvre is executed, to reach a better pointing accuracy, the gain coefficients have to change again. This is due to the fact that the term $\frac{|q_{ie}(0)|}{||q_e(0)||} ||\dot{\theta}_{max}||$ creates unbalanced control torque, which results in a reduced accuracy and noisy angular velocity. When the quaternion error is lower than their normalization of Eq.6.14, both gain $K_i$ and $K_p$ are equal to $J_{tot}$.

### 6.1.4. Tracking

The third control mode considered is the tracking mode. The tracking mode requires the spacecraft to follow a time-dependant attitude over time, performing first a repointing manoeuvre and then to track the attitude. For this control test, the LVLH reference frame has been considered as the target attitude.
Similarly as the previous control modes, the quaternion feedback control, treated as PI control has been chosen to carry out the tracking test, and is expressed by the equation:

$$T_c = -K_i q_e - K_p w_{err} + w_1 \times J w_1 \tag{6.17}$$

Where $w_{err}$ is the error of angular velocity calculated as:

$$w_{err} = w_1 - A_{B/L} w_{lvlh} \tag{6.18}$$

In which $w_{lvlh}$ is the angular velocity of the rotating LVLH frame. Since in this control mode the predominant phase and action of interest is the tracking by itself and not the repointing slew manoeuvre, the slew rate limit was not considered.
For the BSIP case both control gains and the inertia matrix $J$ of the gyroscopic term were

considered equal to $J_1$. For the ASIP case both control gains and the inertia matrix $J$ of the gyroscopic term were considered to be equal to $J_{tot}$.

## 6.2. Control Performance Comparison

To compare the performance of the Before System Identification Procedure and the After System Identification Procedure case, the error on the angular velocity and the attitude error matrix over time have been considered as main parameter, together with the time required to reach the requested performance.

### 6.2.1. Inertial Pointing

For the inertial pointing control mode, two tests have been carried out, each one divided in two different phases. The first test defines a target angular velocity on the x axis in the first phase, while in the second phase the target angular velocity on x axis changes following a parabolic profile. The second test is similar, but the target velocity is a combination of the angular velocities of x,y and z axis. Both tests are aimed at defining the control accuracy of the assembly of satellite considering a simple motion in the first test and a complex one in the second test, due to the presence of the gyroscopic term. Moreover the presence of two phases allows to define the time needed and the available precision to satisfy a certain performance, while the second phase allows to evaluate the delay between the commanded state and the real state of the system.

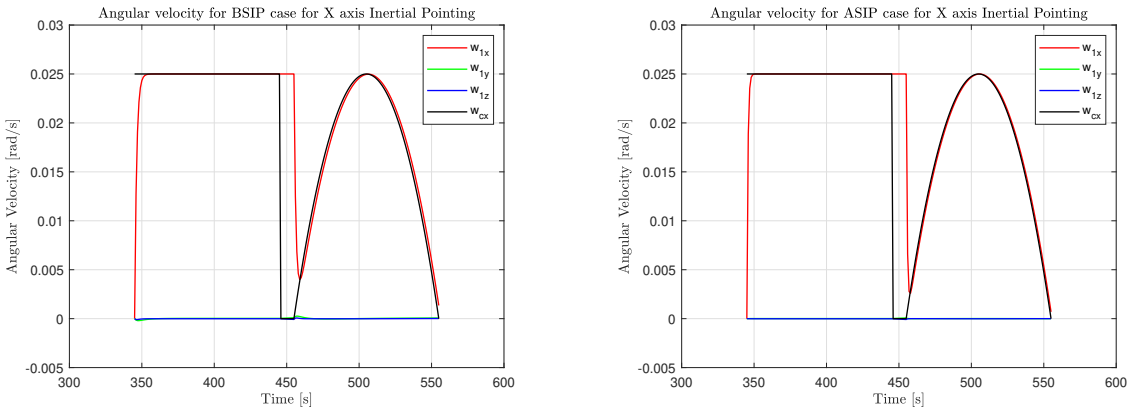


(a) Angular velocity for BSIP case.

(b) Angular velocity for ASIP case.

Figure 6.1: Angular velocity during first inertial pointing test

**X-axis test** The results from the first test in terms of angular velocity and required performance are presented in Fig.6.1a for the BSIP case and in Fig.6.1b for the ASIP case, while for both cases the norm of the error is shown in Fig.6.2.
As expected, it can be seen that both ASIP and BSIP case are able to reach and maintain the required performance, with a better accuracy and a reduced response time for the ASIP case. The faster response time originates from the proportional gain coefficient inside the control law, which allows to deliver greater and more precise torque to the spacecraft from the actuator. The better accuracy during the inertial test can be traced back to the ability of the control law to cancel the gyroscopic term $J_{tot}w_1 \times w_1$ inside the EoM, which acts as a disturbance during the motion. It is interesting to consider that when the target angular velocity changes over time following the parabolic profile, it generates a proportional delay, which results in a loss of accuracy for both cases in a similar manner. This is a direct effect produced by the choice of the control law, and introducing an integral action might reduce this delay effect.

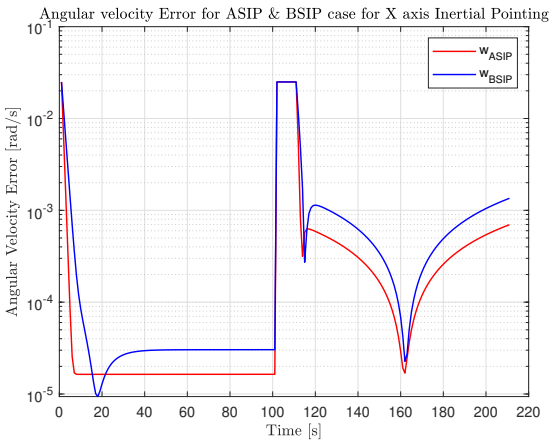


Figure 6.2: Norm of the error for BSIP and ASIP cases during first inertial pointing test

**XYZ axis test** The results from the second test in terms of angular velocity and required performance are presented in Fig.6.3a for the BSIP case and in Fig.6.3b for the ASIP case, while for both cases the norm of the error is shown in Fig.6.4.

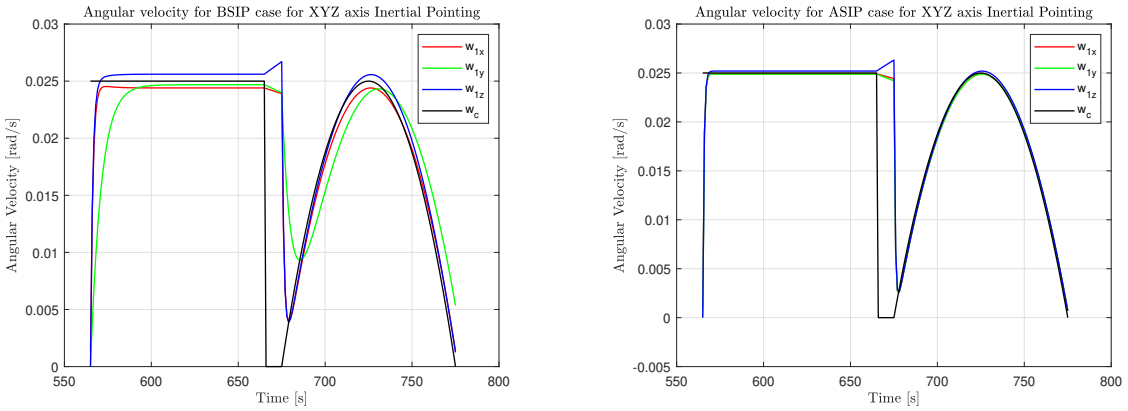


(a) Angular velocity for BSIP case. (b) Angular velocity for ASIP case.

Figure 6.3: Angular velocity during second inertial pointing test

Considering the second inertial pointing control test, the true difference in performance between ASIP and BSIP cases can be assessed. The system identification procedure improves the control accuracy by a order of magnitude and the response time by a couple tens of seconds compared with the BSIP case. Similarly to the first inertia pointing control test, the response time is improved thanks to the increased proportional control gain, which has two functions: it increases and proportionally distributes the control effort delivered by the actuators.

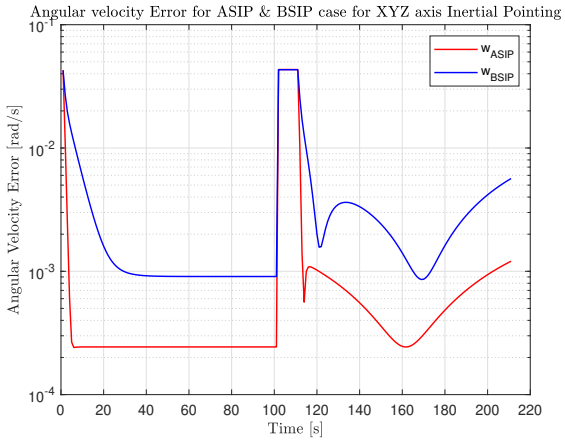


Figure 6.4: Error for BSIP and ASIP cases during second inertial pointing test

This distribution property comes from the nature of the inertia matrix itself, and the BSIP case lacks this property as can be seen in Fig.6.3a, where the angular velocity along y axis presents the most delay compared to x and z axis. The accuracy for the ASIP case is increased, since the full knowledge of $J_{tot}$ allows to cancel the gyroscopic term from the

EoM, which affects the dynamics more and more, being dependant on the combination of angular velocities.

### 6.2.2. Repointing

For the repointing test, a single test has been carried out. To evaluate the pointing accuracy of the spacecraft, the error matrix $A_e$ has been considered:

$$A_e = A_{B/N} A_{S/N}^T \tag{6.19}$$

Since the objective of the control is to make $A_e = I$, the extradiagonal elements of the matrix $A_e$ have been taken into account as measure of the pointing error. The quaternion error vector has been discarded as measure of the error, since the quaternion representation bears no physical meaning. The pointing error as norm of the extradiagonal elements of matrix $A_e$ is reported in Fig.6.5a while the norm on the error of the angular velocity of the first body is shown in Fig.6.5b for both BSIP case and ASIP case.

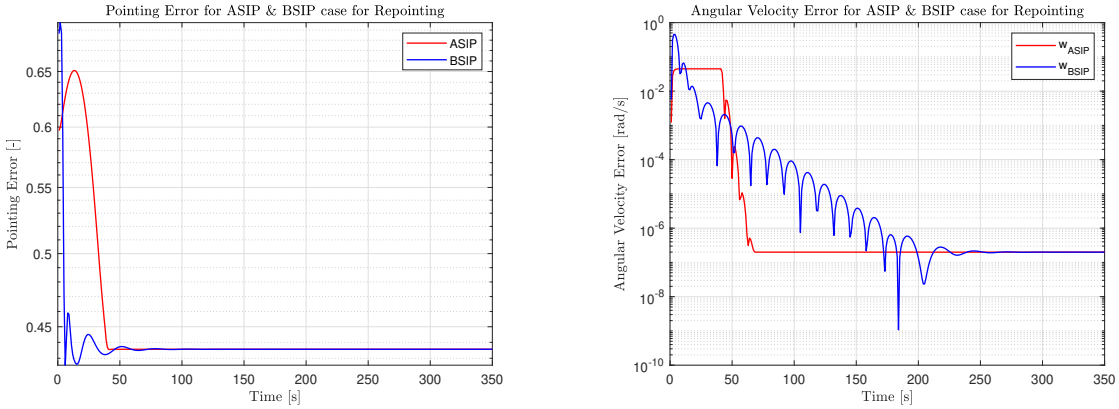


(a) Pointing error

(b) Angular velocity error

Figure 6.5: Pointing accuracy during repointing test

Comparing the angular velocity error and the pointing error, it can be seen that both ASIP case and BSIP case are able to reach the same accuracy level, due to the fact that the control gain chosen for each case are the same for both pointing and angular velocity terms and when a certain accuracy is reached, they cancel each other out. Regarding the response time, it is interesting to notice that even if the ASIP case presents a slew rate limit, it is still able to reach the same level of accuracy in less time than BSIP case, due to the greater control gains employed. Observing Fig.6.5b, and considering the oscillation

pattern, the reduced oscillation for ASIP case is to be found in the ability of the control law to cancel the gyroscopic term, directly related to the data coming from the system identification procedure, which allows for a smoother slew manoeuvre.
To better analyze the behaviour of the spacecraft, the angular velocity of the first body is presented in Fig.6.6a and in Fig.6.6b for the BSIP case and the ASIP case respectively.

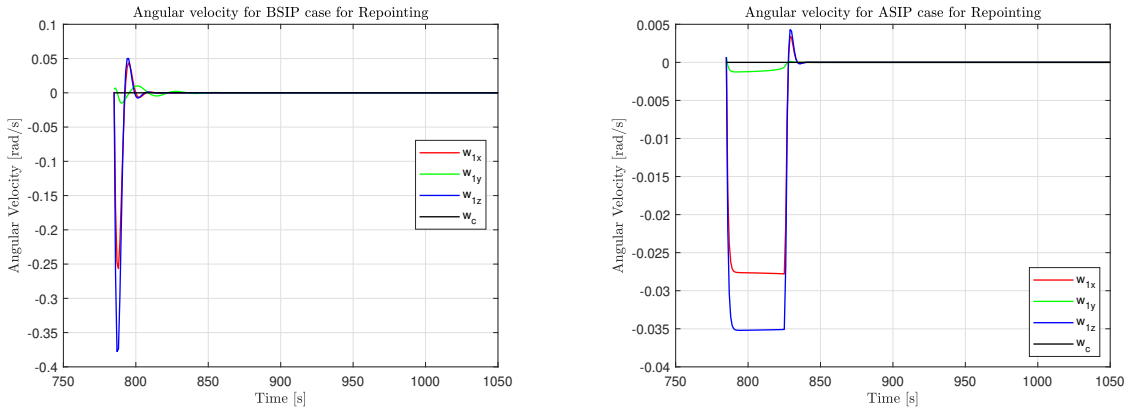


(a) Angular velocity for BSIP case. (b) Angular velocity for ASIP case.

Figure 6.6: Angular velocity during repointing test

It is interesting to notice in Fig.6.6b the presence of a saturation limit in angular velocity, due to the presence of a slew rate limit. Comparing the two images, it can be seen that the angular velocity in the BSIP case is almost an order of magnitude higher than the one in ASIP case, meaning that a greater control torque effort is required to reach the same performance in a longer time.

**Slew rate limit effectiveness** To evaluate the effectiveness of the slew rate limit, the norm of the angular rotation over time has been computed using Eq.6.11 and is showed in Fig.6.7 together with the angular limit chosen before the simulation.
To show the potentiality of such control system, an angular difference of 0.001° has been chosen as upper limit. From the figure it is possible to see that the angular difference is constant and lower that the angular limit during the coasting phase of the slew manoeuvre, while two spikes can be noticed at the beginning and at the end of the manoeuvre. This is an expected behaviour since the spikes correspond to the acceleration and braking phase of the slew manoeuvre, which are not accounted for in the slew rate limit model.

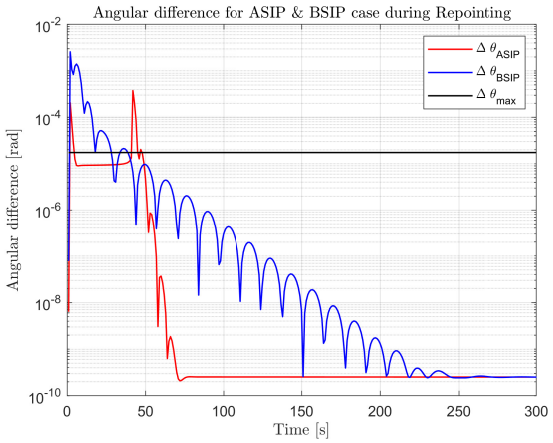


Figure 6.7: Norm of the angular rotation during slew manoeuvre during second inertial pointing test

### 6.2.3. Tracking

The control performance from the tracking control test is expressed in terms of the norm of the angular velocity error and in terms of the norm of the extra-diagonal elements of the error matrix, which in this case is $A_{B/L}$, since the target attitude is the LVLH frame. The results of the test are shown in Fig.6.8a and in Fig.6.8b respectively for both BSIP and ASIP case.

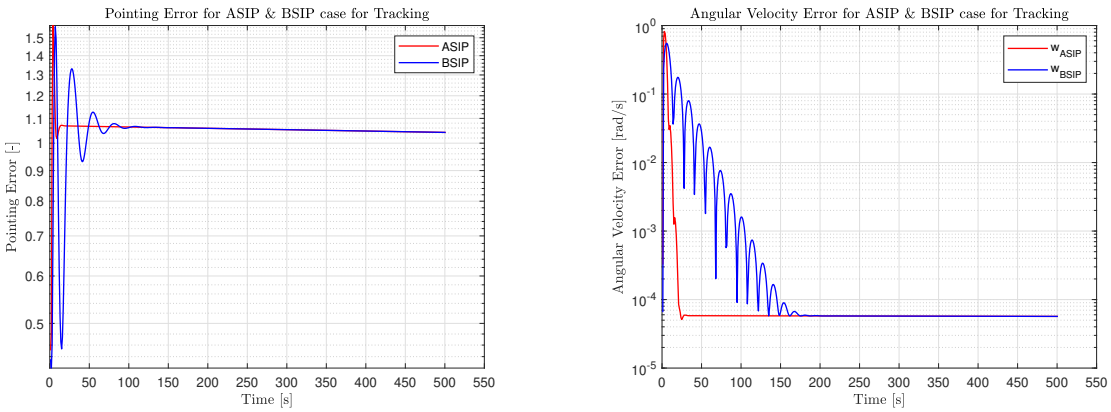


(a) Pointing error

(b) Angular velocity error

Figure 6.8: Pointing accuracy during tracking test

The performance comparison for the tracking control mode is similar to the repointing test. As a matter of fact it can be seen that the only parameter improved by the system identification is the system response and the oscillations around the target performance.

The system response time is improved by using greater and proportionate gains. Regarding the oscillation phenomena, it is rooted in the ability of the control law to cancel the gyroscopic term inside the EoM, only the ASIP case is capable to provide strong cancellation, allowing for an almost smooth reorientation manoeuvre. The accuracy for both cases is the same due to the fact that the control gains for the pointing control term and angular velocity control term inside the control law are the same, and when the pointing error and the angular velocity error are the same, then the control torque is zero.
To gain a better insight on the system behaviour, the angular velocity of the first body is presented in Fig.6.9a for the BSIP case and in Fig.6.9b for the ASIP case.

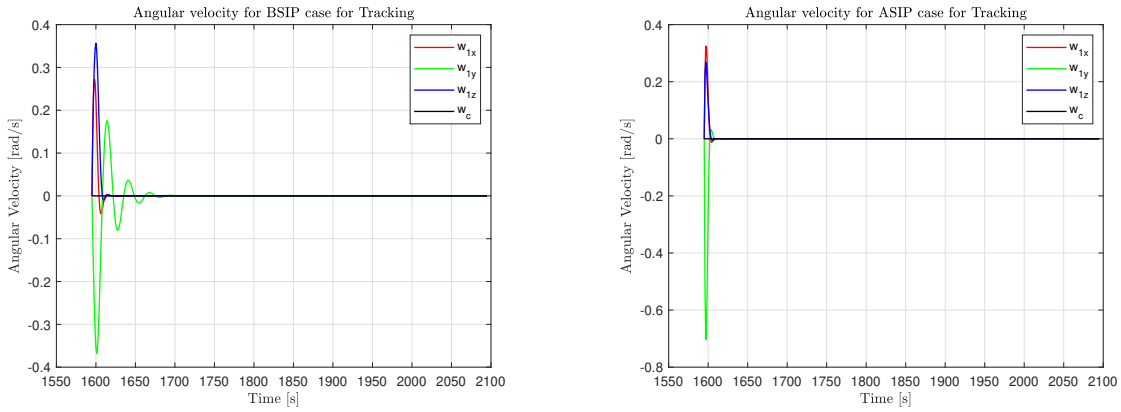


(a) Angular velocity for BSIP case

(b) Angular velocity for ASIP case

Figure 6.9: Angular velocity during tracking test

The angular velocities presented in these two figure allow to make some considerations regarding the torque and the general behaviour of the spacecraft. As in the previous test, for the BSIP case the angular velocity on y-axis presents the largest amplitudes, and reaches as last the target angular velocity. On the contrary, for the ASIP case all angular velocity components reach simultaneously the target angular velocity. This behaviour can be explained considering the control gains used, specifically the inertia matrix values, which allows the use of adequate and distributed torque to reach the control objective.

# Conclusions & Future Development

The present Work aimed at studying the system identification process of two satellites after the docking by the means of computer simulation. As case study, the on Orbit Servicing mission between the MEV-1 and Intelsat-901 was taken into consideration, and a procedure of system identification has been created considering both analytic and numerical method. The rigid body model has been chosen to carry out the simulation and a white box model has been considered for the system identification procedure. The first phase of the procedure generates a coarse estimation of the inertia matrix of the whole assembly through analytical consideration of the EoM, the estimation is then is refined during the second phase using a NLP technique. In the third phase the position of the center of mass for the whole assembly is assessed by analytical method, which allows to define the inertia matrix of each satellite in the fourth phase. In the fifth phase of the system identification procedure, a least-squares algorithm is used to identify the mechanical properties of the link between spacecrafts in terms of visco-elastic coefficients. The procedure was then used to estimate the mass properties of the MEV-1 & Intelsat-901 assembly in different environmental conditions and established the dependency between environmental conditions and estimation accuracy. To assess the robustness of the system identification procedure, a sensitivity analysis has been carried out, which resulted in a strong relationships between estimation accuracy, knowledge of the input torque and quality of the angular velocity profile. Lastly a performance comparison in the form of a control test has been carried out to compare the ability to control the assembly of spacecrafts before and after the system identification procedure. The control test certified an improvement in terms of time response after the system identification in each control mode, and a significant improvement in accuracy only for inertial pointing mode.
Considering future developments, to improve the system identification procedure, additional phases with increasing complexity in dynamical model may be added to estimate also the inertia matrices of the appendages, such as solar arrays, antennas or other platforms. Alternatively, the estimation of disturbances as the sloshing mass, may be integrated in future developments. Moreover more elements characterizing the spacecraft ADCS, as sensors and actuators could be implemented to study specific cases.

# Bibliography

[1] Arianespace. Arianespace launchkit intelsat-901, 2001.

[2] Arianespace. Arianespace today lofted the intelsat 901 satellite for the intelsat telecommunications organization, 2001. URL `https://www.defense-aerospace.com/ariane-launches-intelsat-satellite-june-11/`.

[3] R. Bordany, W. Steyn, and M. Crawford. In-orbit estimation of the inertia matrix and thruster parameters of uosat-12. 2000.

[4] W. Chen and Q. Hu. Sliding-mode-based attitude tracking control of spacecraft under reaction wheel uncertainties. *IEEE/CAA Journal of Automatica Sinica*, pages 1–13, 2022. doi: 10.1109/JAS.2022.105665.

[5] DARPA. Orbital express fact sheet, 2007.

[6] ESA. Mev-1 & 2 (mission extension vehicle-1 and -2), 2020. URL `https://www.eoportal.org/satellite-missions/mev-1#spacecraft`.

[7] A. Flores-Abad, M. Nandayapa, and M. A. Garcia-Teran. Force sensorless impedance control for a space robot to capture a satellite for on-orbit servicing. In *2018 IEEE Aerospace Conference*, pages 1–7. IEEE, 2018.

[8] N. Geographic. The secret to hubble's success, 2015. URL `https://web.archive.org/web/20150428040059/http://www.nationalgeographic.com/hubble-timeline/`.

[9] D. C. Howard. *Orbital Mechanics for Engineering Students*. Elsevier aerospace, 2005.

[10] Q. Hu, B. Li, X. Huo, and Z. Shi. Spacecraft attitude tracking control under actuator magnitude deviation and misalignment. *Aerospace Science and Technology*, 28(1): 266–280, 2013.

[11] Ilslaunch. E5wb/mev-1 mission overview, 2019.

[12] Intelsat. Northrop grumman successfully completes historic first docking of mission extension vehicle with intelsat 901 satellite, 2020.

[13] B.-E. Jun, D. S. Bernstein, and N. H. McClamroch. Identification of the inertia matrix of a rotating body based on errors-in-variables models. *International journal of adaptive control and signal processing*, 24(3):203–210, 2010.

[14] T. Kasai, I. Yamaguchi, H. Igawa, S. Mitani, T. Ohtani, M. Ikeda, and K. Sunagawa. On-orbit system identification experiments of the engineering test satellite-viii. *TRANSACTIONS OF THE JAPAN SOCIETY FOR AERONAUTICAL AND SPACE SCIENCES, SPACE TECHNOLOGY JAPAN*, 7(ists26):Pc_79–Pc_84, 2009.

[15] J. Keim, A. Behcet Acikmese, and J. Shields. Spacecraft inertia estimation via constrained least squares. In *2006 IEEE Aerospace Conference*, pages 6 pp.–, 2006. doi: 10.1109/AERO.2006.1655995.

[16] A. Kutlu, C. Haciyev, and O. Tekinalp. Attitude determination and rotational motion parameters identification of a leo satellite through magnetometer and sun sensor data. In *2007 3rd International Conference on Recent Advances in Space Technologies*, pages 458–461. IEEE, 2007.

[17] L. Ljung. Perspectives on system identification. *Annual Reviews in Control*, 34(1): 1–12, 2010.

[18] NASA. Spacecraft thermal control coatings references, 2005. For spacecraft body SRP coefficients.

[19] NASA. Distribute spacecraft autonomy (dsa), 2020. URL `https://www.nasa.gov/directorates/spacetech/game_changing_development/projects/dsa`.

[20] I. A. of Geomagnetism and Aeronomy. Igrf online page. URL `https://www.ngdc.noaa.gov/IAGA/vmod/igrf.html`.

[21] OrbitalFocus. Mev-1 and intelsat 901 orbtial data, 2023. URL `https://www.orbitalfocus.uk/Diaries/US/MEV1.php`.

[22] K. Schittkowski. *Numerical data fitting in dynamical systems: a practical introduction with applications and software*, volume 77. Springer Science & Business Media, 2002.

[23] J. L. Schwartz and C. D. Hall. Comparison of system identification techniques for a spherical air-bearing spacecraft simulator. *Advances in the Astronautical Sciences*, 116:1725–1741, 2004.

[24] J. Sjöberg, Q. Zhang, L. Ljung, A. Benveniste, B. Delyon, P.-Y. Glorennec, H. Hjal-

marsson, and A. Juditsky. Nonlinear black-box modeling in system identification: a unified overview. *Automatica*, 31(12):1691–1724, 1995.

[25] SPECTROLAB. Space solar panels. How it was published, 7 2010. For spacecraft panels SRP coefficients.

[26] J. R. Wertz. *Spacecraft Attitude Determination and Control*. KLUWER ACADEMIC PUBLISHERS, 2002.

[27] B. Wie. *Space Veichle Dynamics and Control*. American Institute of Aeronautics and Astronautics, Inc, 2008.

[28] B. Xiao, Q. Hu, D. Wang, and E. K. Poh. Attitude tracking control of rigid spacecraft with actuator misalignment and fault. *IEEE Transactions on Control Systems Technology*, 21(6):2360–2366, 2013. doi: 10.1109/TCST.2012.2237403.

[29] B. Xiao, Q. Hu, D. Wang, and E. K. Poh. Attitude tracking control of rigid spacecraft with actuator misalignment and fault. *IEEE Transactions on Control Systems Technology*, 21(6):2360–2366, 2013.

[30] H. Yoon and P. Tsiotras. Adaptive spacecraft attitude tracking control with actuator uncertainties. *The Journal of the Astronautical Sciences*, 56(2):251–268, 2008.

[31] H. Yoon, Y. Eun, and C. Park. Adaptive tracking control of spacecraft relative motion with mass and thruster uncertainties. *Aerospace Science and Technology*, 34: 75–83, 2014.